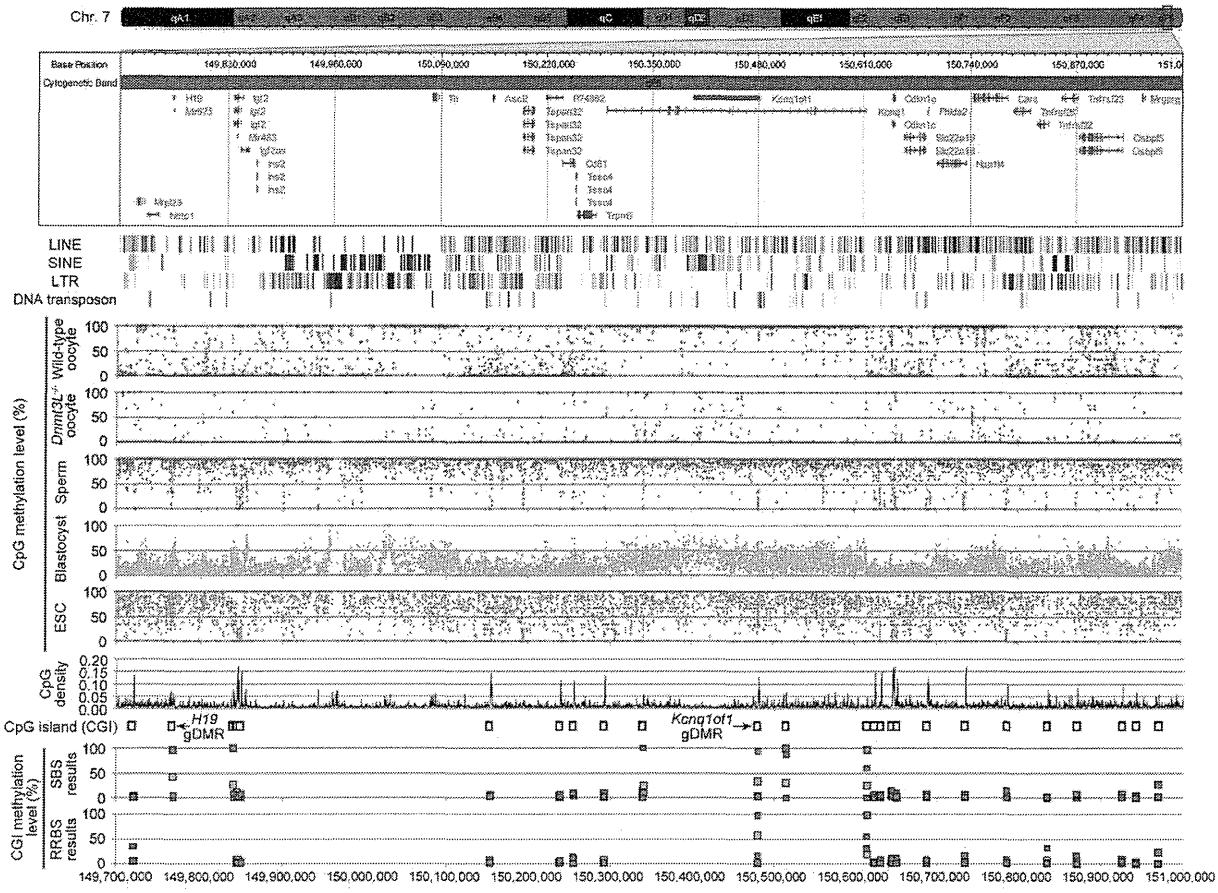

Figure 1. High-resolution DNA methylome map of mouse distal chromosome 7 imprinting cluster. Illumina GenomeStudio viewer displays the locations of genes in distal chromosome 7 (149,700,000–151,000,000). Black vertical bars represent the location of 4 repetitive elements: LINE, SINE, LTR, and DNA transposons. Red, purple, blue, green, and khaki dots represent the methylation levels at individual CpGs in wild-type oocyte, *Dnmt3L*$^{-/-}$ oocyte, sperm, blastocyst, and ESC genomes, respectively. Black line plots depict the distribution of CpG densities (number of CpG per 200 nt) of individual CpGs. Open boxes represent the location of CpG islands (CGIs). Red, purple, blue, and green boxes represent the methylation levels at individual CGIs in wild-type oocyte, *Dnmt3L*$^{-/-}$ oocyte, sperm, and blastocyst genomes, respectively, determined by our results from shotgun bisulfite sequencing (SBS) method and Smallwood's results from reduced representation bisulfite sequencing (RRBS) method [38].
doi:10.1371/journal.pgen.1002440.g001

Dnmt3L$^{-/-}$ oocytes (4.4%) was lower than that observed in wild-type oocytes (6.6%). Sperm methylation levels, by comparison, were relatively high (14.7%), whereas those of the blastocysts and ESCs were quite low (1.3% and 2.1%, respectively) (Figure S4).

Since previous studies revealed a significant correlation between CpG frequency and methylation within intra- and intergenic regions in somatic cells [32,33], the CpG density and methylation levels were compared to identify genome-wide differential methylation patterns in germ cells. CpG density was defined as the number of CpG dinucleotides in 200 nucleotide (nt) windows (*e.g.*, 1 CpG dinucleotide per 200 nt corresponds to a density of 0.005). At low CpG densities (range, 0.005–0.05), the oocyte genome was about 50% methylated, whereas the sperm genome was 80–90% methylated. At moderate to high CpG densities (range, 0.05–0.2), both male and female germ cells were hypomethylated (Figure 2B). Furthermore, 4 families of transposable elements (long interspersed nuclear elements (LINEs), short interspersed nuclear elements (SINEs), long terminal repeats (LTRs), and DNA transposons) were moderately methylated in oocyte genomes but were hypermethylated in sperm. In addition, a general trend towards higher methylation levels at higher CpG densities in the oocyte genome occurred in LTRs. Conversely, a trend toward lower CpG methylation levels at higher CpG densities in the wild-type oocyte and sperm genomes was observed in SINEs and DNA transposons. In contrast, all of these transposable elements were hypomethylated in *Dnmt3L*$^{-/-}$ oocytes. Interestingly, however, there was partial CpG methylation in LINEs and LTRs at relatively high CpG densities (range, 0.03–0.1). These complete or partial under-methylations were confirmed by bisulfite sequencing in L1 LINEs, B1/Alu SINEs, and intracisternal A particle (IAP) LTRs (Figure S7). These results suggested that each germ cell has a unique sequence- and CpG-density-dependent methylation pattern. In addition, oocyte CpG methylation, except in a subset of retrotransposons, appears to be *Dnmt3L* dependent.

We also characterized the methylation patterns of 15 germline-differentially methylated regions (gDMRs). The differential (between oocyte and sperm) methylation occurs at imprinted gene loci (also called imprinting control regions (ICRs)). The ICRs of maternally methylated imprinted genes (*e.g.*, *Nespas-Gnas*) were shown to be hypermethylated in oocytes but hypomethylated in sperm, while the converse was true in ICRs of paternally-methylated imprinted genes (*e.g.*, *H19*) (Figure 3 and Figure S8). Interestingly, only the *Snrpn*

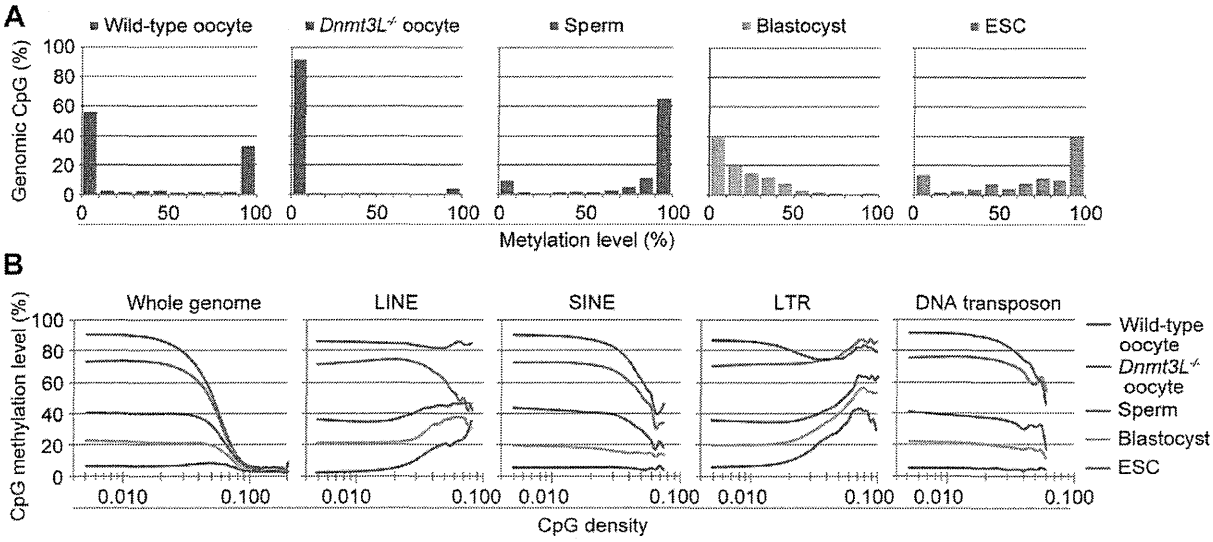

Figure 2. Genome-wide methylation profiling of mouse germ cells. (A) Histograms of methylation levels of genomic CpGs in wild-type oocyte, *Dnmt3L*$^{-/-}$ oocyte, sperm, blastocyst, and embryonic stem cell (ESC) genomes. (B) CpG methylation levels are plotted as a function of CpG density for the whole genome and 4 families of transposable elements (long interspersed nuclear element (LINE), short interspersed nuclear element (SINE), long terminal repeat (LTR), and DNA transposon).
doi:10.1371/journal.pgen.1002440.g002

gDMR was partially methylated (35.7%), whereas all other maternal ICRs were hypomethylated in *Dnmt3L*$^{-/-}$ oocytes (Table 2). This residual methylation might result in the stochastic acquisition of the maternal imprint in the progeny of *Dnmt3L*$^{-/-}$ females [34]. These results strongly suggested that the methylation level of individual CpGs can be determined from DNA methylome maps with a high degree of accuracy.

The study of mammalian DNA methylation patterns has previously suggested that methylation predominantly occurs at CpG sites; however, more recent studies, based on SBS methods, have indicated that methylation at non-CpG sites also occurs in human ESCs [22,23]. Detection of non-CpG methylation is one of the applications of the bisulfite-based methylation analysis but is problematic due to the incomplete conversion of cytosine, and overestimates of such cytosine by PCR amplification, which cannot be discriminated from true methylation. In order to evaluate the methylation status of non-CpG sites and avoid these problems, additional SBS analysis of mouse GV oocytes, sperm, blastocysts, and ESCs was performed by a non-amplification technique, termed Post-Bisulfite Adapter Tagging (PBAT) [Miura F. & Ito T, personal communication]. All C (originally methylated cytosine) and T (originally unmethylated cytosine) that mapped to genomic CpG and CpH sites (H = A, T, or C) were counted. The PBAT results showed CpG methylation ratios (C ratios = 0.395, 0.748, 0.137, 0.615 in oocytes, sperm. blastocysts, and ESCs) which are similar to the average methylation levels of individual DNA methylome maps obtained by MethylC-seq and WBA-seq among all examined cells. Interestingly, a relatively high fold enrichment of non-CpG methylation was observed in GV oocytes (C ratio = 0.034–0.038), but not in the other cell types, including mouse ESCs (C ratio <0.01) (Figure S11).

Relationship between the DNA methylome and transcriptome of mouse germ cells

To elucidate the interaction between intragenic DNA methylation and gene transcription, the correlation between promoter and gene-body methylation and expression levels for 20,854 different genes was examined. The mRNA-seq profiles for germ cells and ESCs are shown in Table S1. The results showed that mRNA transcript levels in oocytes were strongly correlated to gene-body methylation levels (Spearman's $\rho > 0.5$, $p < 1 \times 10^{-9}$) but were not significantly correlated to promoter methylation levels ($|\rho| < 0.1$) (Figure 4A). For example, the regions +2 to +5 kb from the transcription start site (TSS) and 0 to −5 kb from the transcription termination site (TTS) were hypermethylated (60–90% methylation) for the top 20% of expressed genes but were hypomethylated (10–30% methylation) for the bottom 20% of expressed genes. However, areas near the TSS (±500 base pairs (bp)) were hypomethylated (10–20% methylation) in all genes, regardless of their expression level. In contrast, in the *Dnmt3L*$^{-/-}$ oocyte genome, the correlation between gene expression and gene-body methylation was very weak ($|\rho| < 0.1$) (Figure 4B). In the sperm genome, promoter methylation was negatively correlated (Spearman's $\rho = -0.36$, $p < 1 \times 10^{-9}$) with gene expression, whereas gene-body methylation was positively correlated (Spearman's $\rho = 0.14$–0.16, $p < 1 \times 10^{-9}$) to gene expression; the latter correlation was weaker than that observed in the oocyte genome (Figure 4C).

Role of *Dnmt3L* in the DNA methylome/transcriptome relationship

Further investigation of gene expression patterns in oocyte genomes revealed that the mRNA transcript levels between wild-type and *Dnmt3L*$^{-/-}$ oocytes were very highly correlated ($R^2 = 0.9611$) (Figure 5A). In fact, there were no significant differences in the expression levels of representative oocyte-specific genes (*e.g.*, *Gdf9*, *Bmp15*, *Bcl2l10*, *Zp1*, *Zp2*, *Zp3*, *Zar1*, *Npm2*, *Nlrp5*, and *Dppa3*, which are responsible for ovarian follicle formation, reproduction, and early development [35]) and DNA methyltransferase genes (*e.g.*, *Dnmt1*, a maintenance methyltransferase, and *Dnmt3a* and *Dnmt3b de novo* methyltransferases); the expected difference in the expression level of *Dnmt3L* between wild-type and

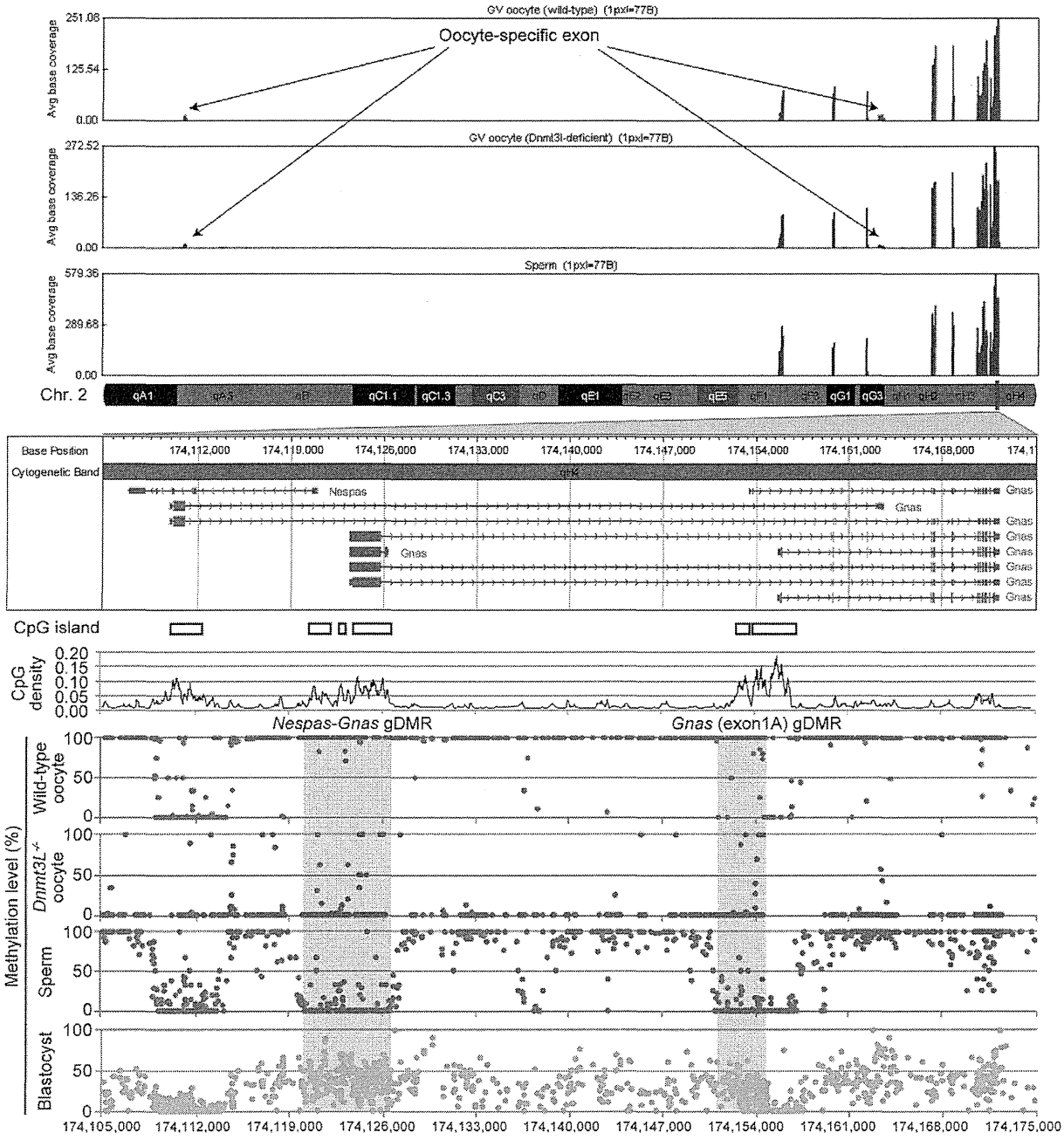

Figure 3. High-resolution genome-wide mRNA expression and CpG methylation profiling. GenomeStudio view of mRNA-seq data and CpG methylation map of the genomic region spanning the *Nespas-Gnas* maternally imprinted locus. (*Top*) Genomic stacked alignment plots of wild-type oocytes, *Dnmt3L*$^{-/-}$ oocytes, and sperm. (*Middle*) Open boxes and black line plots represent the location of CGIs and the distribution of CpG densities of individual CpGs, respectively. (*Bottom*) Red, purple, blue, and green dots represent the methylation levels at individual CpGs in wild-type oocyte, *Dnmt3L*$^{-/-}$ oocyte, sperm, and blastocyst genomes, respectively. The red shaded areas show the extent of two maternal imprinting control regions (ICRs).
doi:10.1371/journal.pgen.1002440.g003

Dnmt3L$^{-/-}$ oocytes was observed (Figure 5B, 5C). These results suggested that changes in gene expression did not occur during oogenesis, despite global intragenic hypomethylation in *Dnmt3L*$^{-/-}$ oocytes. Furthermore, the expression levels and exon patterns of maternally-methylated imprinted genes across each ICR were not altered in *Dnmt3L*$^{-/-}$ oocytes (Figure 3 and Figure 5D). This result suggested that the disruption of maternal methylation imprints in the *Dnmt3L*$^{-/-}$ oocyte genome was not due to the lack of their transcription [36]. On the other hand, maternal methylation imprints at ICRs (and many other hypermethyla-

Table 2. CpG methylation profiling of 12 maternal and 3 paternal imprinting control regions.

	Gene locus	Chr.	Extents of the ICRs†		Average methylation levels				
			Start	End	Wild-type oocyte	*Dnmtl1*$^{-/-}$ oocyte	Sperm	Blastocyst	ESC
Maternally methylate imprinted genes	*Nespas-Gnas*	2	174,119,863	174,126,564	99.3%	5.6%	3.9%	38.2%	55.9%
	Gnas (exon1A)	2	174,150,877	174,154,638	95.2%	3.5%	4.1%	20.4%	7.8%
	Peg10	6	4,696,743	4,699,483	95.9%	6.7%	5.5%	31.8%	57.1%
	Mest	6	30,684,932	30,689,966	96.5%	2.3%	4.2%	30.7%	52.6%
	Peg3	7	6,679,787	6,684,257	98.1%	3.0%	2.5%	32.1%	42.8%
	Snrpn	7	67,147,381	67,151,583	94.1%	35.7%	4.6%	34.3%	64.9%
	Kcnq1ot1	7	150,480,736	150,482,810	97.9%	2.2%	4.3%	34.1%	52.0%
	Plagl1	10	12,809,697	12,812,131	99.9%	1.3%	7.4%	35.4%	53.0%
	Grb10	11	11,925,127	11,927,100	98.0%	1.2%	5.3%	38.5%	78.7%
	Zrsr1	11	22,871,610	22,874,212	94.1%	5.2%	6.8%	34.8%	47.0%
	Igf2r	17	12,934,169	12,935,816	99.1%	0.9%	3.8%	44.2%	53.2%
	Impact	18	13,130,435	13,133,510	97.2%	2.4%	6.6%	43.1%	38.6%
Paternally methylated imprinted genes	*H19*	7	149,764,673	149,771,930	13.5%	0.6%	96.5%	40.8%	65.5%
	Rasgrf1	9	89,767,090	89,775,128	7.4%	0.7%	92.0%	25.2%	59.4%
	Dlk1-Meg3	12	110,762,703	110,773,093	18.9%	0.9%	96.8%	32.4%	83.1%

†: The extents of each region in germ cells were determined by bisulfite sequencing study [39].

doi:10.1371/journal.pgen.1002440.t002

tions at transcribed regions) in wild-type oocyte genomes might be the result of gene transcription via *Dnmt3L*-mediated intragenic methylation.

Surprisingly, gene expression in ESC genomes was negatively correlated with promoter methylation and was not positively correlated with gene-body methylation (Figure S12). Meanwhile, these ESCs showed the apparent expression of all DNA methyltransferase gene families including *Dnmt3L* (Figure S13). Previous studies indicated that the zygotic and somatic functioning of *Dnmt3L* is not essential for global methylation in ESCs in mice [6]. Thus, unlike oocytes, the functional role of *Dnmt3L* in gene-body methylation after fertilization is unclear. However, the expression of pluripotency-associated genes, *Pou5f1*, *Klf4*, *Sox2*, *Myc*, *Nanog*, and *Lin28a*, was clearly observed in ESCs. The expression of *Pou5f1*, *Lin28a*, and *Glis1*, recently identified as maternal reprogramming factors, were also observed in oocytes (Figure S14). While differential expression of the pluripotency genes among germ and stem cells was observed, the promoter regions of these genes demonstrated low-level methylation in almost all of the examined cells. In sperm cells, only the *Nanog* promoter was hypermethylated (this result was similar to a previous study [29]).

Identification and characterization of germline differentially methylated regions

To identify gDMRs, the average CpG methylation levels of individual CpG islands (CGIs), which are CpG-rich genomic regions often lacking DNA methylation, were calculated. Recently, Illingworth et al. determined the number of CGIs by deep sequencing of isolated, unmethylated DNA clusters [37]. Among the 23,021 mouse CGIs (22,974 CGIs were informative in both oocytes and sperm), 2014 were highly methylated (≥80% methylation) in oocytes, 818 were highly methylated in sperm, and 377 were highly methylated in both germ cells (Figure 6A). Furthermore, we also identified 1678 gDMRs (≥80% methylation in 1 gamete and ≤20% in the other), 1329 of which were oocyte-specific methylated CGIs, while the remaining 349 were sperm-specific methylated CGIs (Figure 6A, Figure S6, and Table S2). Among these gDMRs, 646 gDMRs were confirmed to show a differential methylation status between GV oocytes and sperm (by similar criteria: ≥75% methylation in 1 gamete and ≤25% in the other); the methylation status was previously examined by performing large-scale bisulfite sequencing of CpG-rich regions of the genome (reduced representation bisulfite sequencing: RRBS) (Table S3) [38]. Additionally, almost all known ICRs except *Zdbf2* DMRs (which do not have any CGIs) were re-identified from our gDMR list (Table S2).

A total of 78% oocyte-methylated gDMRs (n = 1045) were located within the intragenic regions. Approximately 25% of the oocyte-methylated gDMRs (n = 322) overlap with either the first exon or the proximal promoter regions of the genes, as has been observed with most of the described maternal ICRs [39]; only 5% of the sperm-methylated gDMR (n = 18) showed such overlap. Alternatively, 34% of sperm-methylated gDMRs (n = 120) overlap with intergenic regions, as in all known paternal ICRs (Figure 6B). Interestingly, oocyte-methylated gDMRs in transcribed regions tended to be more abundant within highly expressed genes, but such a trend was not observed in the sperm genome (Figure 6C). Oocyte-methylated gDMRs were also identified in non-imprinted genes, such as the DNA methyltransferase genes (*e.g.*, *Dnmt1* and *Dnmt3b*) and some male germline-specific genes (*e.g.*, *Piwil1*, *Spag1*, *Cgnbp2*, *Tbpl1*, *Spata16*, *Cgn*, *Acrbp*, and *Cd46*). The oocyte-methylated gDMR in *Dnmt1* was located in spermatocyte- and somatic-specific exons, while oocyte-specific exons were hypomethylated in oocytes (Figure S9). *Dnmt3L*$^{-/-}$ oocytes also showed hypomethylation in most of these gDMRs. Significant changes in the expression levels of genes with alternative splicing patterns were not observed in the *Dnmt3L*$^{-/-}$ oocyte genome (Figure 3, Figure 5E, and Figure S9). These results indicate that these oocyte-specific methylated gDMRs do not regulate gene expression or alternative splicing during the oocyte stage.

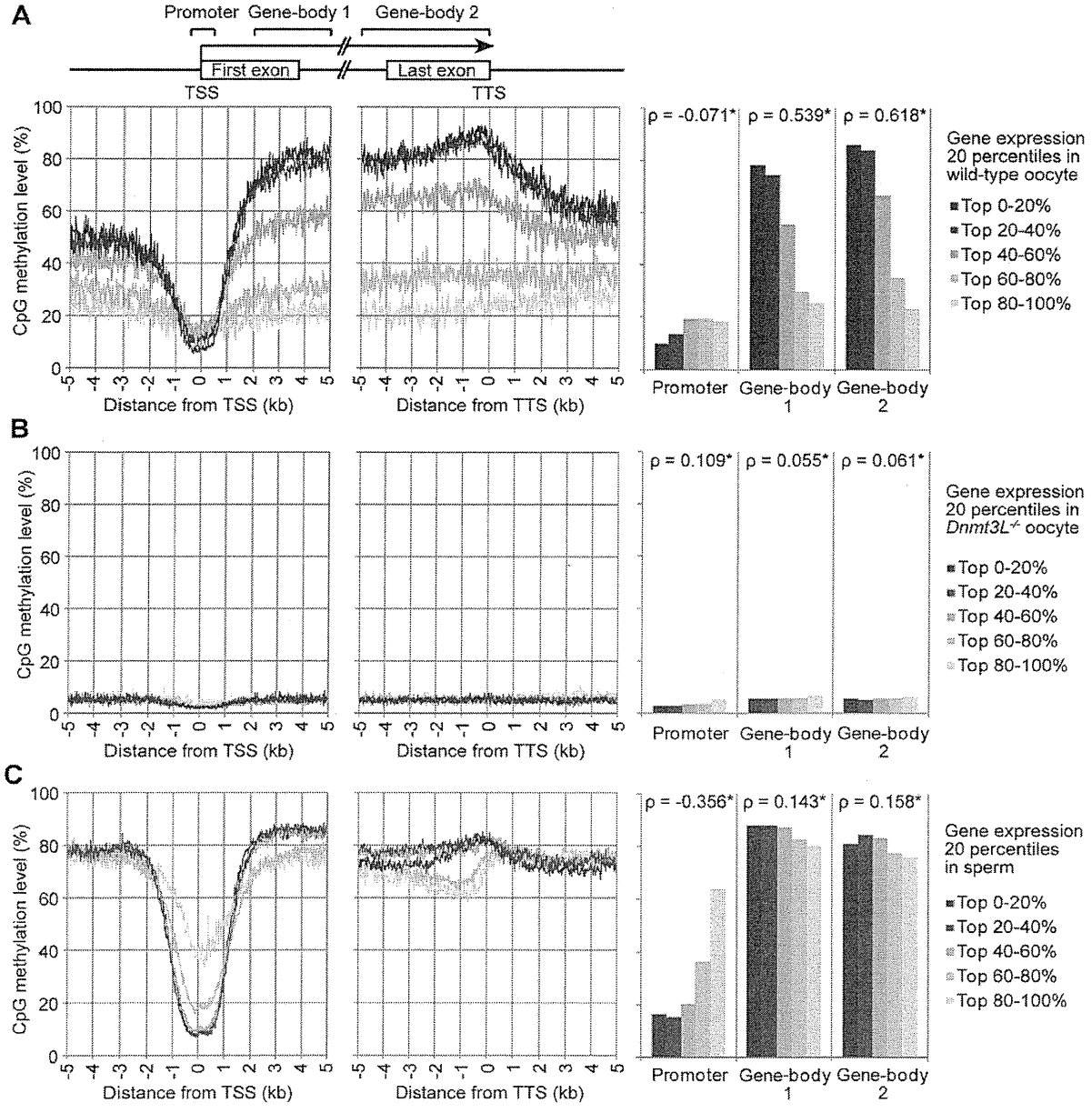

Figure 4. Relationship between gene expression and methylation in promoter and gene-body regions in mouse germ cells. The expression level of genes in wild-type oocytes (A), sperm (B), and *Dnmt3L*$^{-/-}$ oocytes (C) were divided into 5 percentile groups. The distribution of methylation is shown ±5 kb from the transcription termination site (TTS; *left*) and transcription start site (TSS; *middle*). The graphs on the right show the average methylation levels in the promoter and gene-body regions. Spearman's rank correlation coefficient (ρ) was used to test the statistical significance of the correlation between gene expression and DNA methylation levels (*: $p<1\times10^{-9}$).
doi:10.1371/journal.pgen.1002440.g004

To determine whether or not these germ cell-specific methylations are maintained after fertilization, when the genomes undergo global demethylation, the individual CGI methylation levels in blastocyst genomes were calculated. In blastocysts, all ICRs demonstrated low to moderate methylation (25.1–64.3%), whereas many gDMRs were demethylated (0–20%) (Figure 6D). Furthermore, 817 oocyte-methylated gDMRs (including *Piwil1*, despite being a non-imprinted gene locus) and 34 sperm-specific gDMRs were resistant to demethylation during early embryogenesis (≥20% methylation in blastocysts) (Figure 6D and Table S2). Among the demethylation-resistant gDMRs, a novel gDMR in the intron of *Gpr1* (Figure S10) was found to be a tissue-specific, paternally-expressed imprinted gene [40]. Bisulfite sequencing analysis showed that this gDMR was hypomethylated in *Dnmt3L*$^{-/-}$ oocytes and maternal allele-specific methylation was detected in this region in blastocysts (Figure 6E). Methylation profiles in ESCs showed that 26% (n = 213) of the demethylation-resistant gDMRs became less methylated (0–20%) whereas the other gDMRs maintained or increased DNA methylation (Figure S15). Among ICRs, only *Gnas* exon1A ICR was demethylated (7.8%),

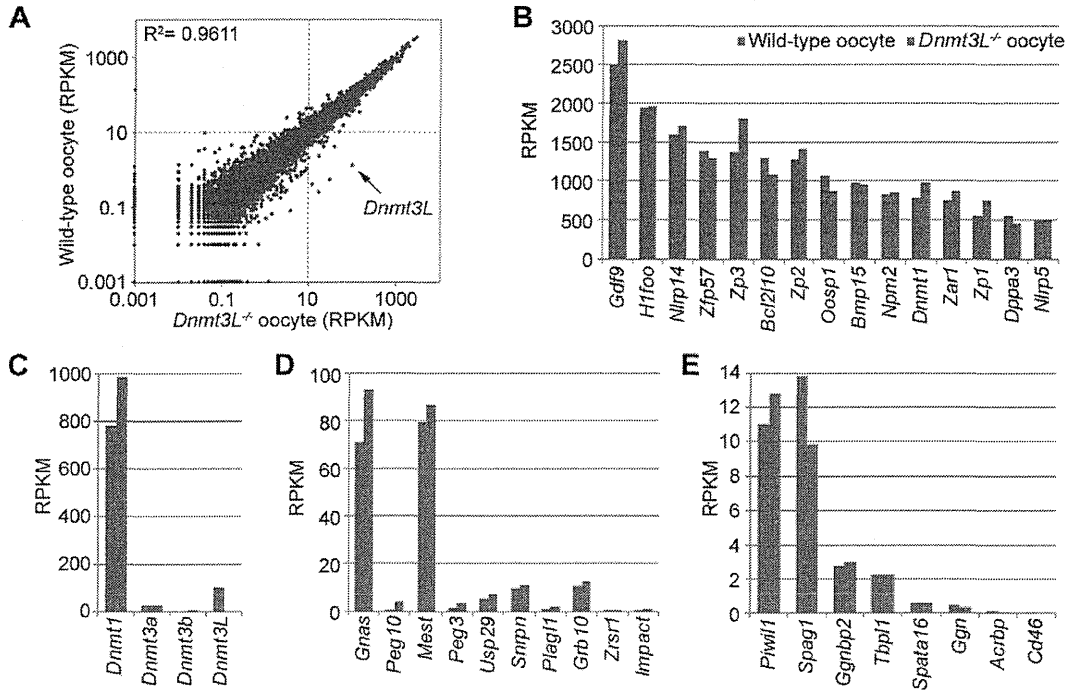

Figure 5. Comparison of gene expression profiles between wild-type and *Dnmt3L*$^{-/-}$ oocytes. (A) Scatter plot and correlation coefficient (R^2) of RPKM values of 20,854 genes in wild-type and *Dnmt3L*$^{-/-}$ oocytes. Expression levels of oocyte-specific genes (B), DNA methyltransferase genes (C), maternally-imprinted genes that are potentially necessary to establish methylation imprints (D), and male germline-specific genes that contain oocyte-specific methylated CpG islands (CGIs) (E).
doi:10.1371/journal.pgen.1002440.g005

whereas the other ICRs developed partial or high methylation levels (range, 38.6–83.1%) in ESCs (Table 2). Among other demethylation-sensitive gDMRs, which were demethylated (<20% methylation) in blastocysts, many (76%, n = 264) sperm-methylated gDMRs were re-methylated (≥20% methylation); most (81%, n = 416) of the oocyte-methylated gDMRs maintained low methylation (0–20%) in ESCs (Figure S15). Finally, out of 704 demethylation-resistant (in blastocysts) oocyte-methylated gDMRs which were informative in *Dnmt3L*$^{-/-}$ oocytes, only 4 remained hypermethylated (80–100% methylation) in the *Dnmt3L*$^{-/-}$ oocyte genome. However, almost all other oocyte-specific methylation marks at gDMRs were *Dnmt3L*-dependent (Figure 6F). These results suggest that *Dnmt3L*-mediated methylation during oogenesis regulates the establishment of most heritable oocyte-specific marks, including genomic imprints.

Discussion

To the best of our knowledge, this is the first study to generate single-base resolution maps of DNA methylomes spanning the entire genome of mouse germ cells. The oocyte maps are particularly valuable and informative because, in the past, such an analysis was prohibitive due to the need for large quantities of DNA. Recently, Smallwood et al. [38] reported large-scale DNA methylation patterns in mouse germ cells by using the RRBS method, which targets only CpG-rich regions. However, our more comprehensive results provide strong evidence that gene expression was positively correlated to *Dnmt3L*-dependent intragenic methylation in oocytes, and that methylation patterns in oocytes differed from those in sperm and non-germline cells.

The functional role of gene-body methylation has been an enigma despite its conservation in plants and animals [41–43]. Maunakea et al. [44] suggested that gene-body methylation is involved in the regulation of alternative splicing events. Although methylated gDMRs were detected in the alternative exons of *Dnmt1* and *Gnas* in mouse oocytes, loss of oocyte-specific methylation marks in the *Dnmt3L*$^{-/-}$ oocytes did not affect the expression patterns of alternatively spliced transcripts. Therefore, our results indicate that gene-body methylation is not involved in alternative splicing in oocytes.

Previously, Chotalia et al. [36] showed that transcription during the oocyte stage is required for the establishment of maternal methylation marks on an imprinted gene. The present results show that *Dnmt3L*$^{-/-}$ oocytes lost almost all of their maternal methylation imprints while maintaining a constant amount of mRNA through each ICR despite the global loss of intragenic methylation. Thus, these results strongly suggest that the establishment of genomic imprints via transcription is mediated by *Dnmt3L*-dependent intragenic methylation.

A possible mechanism for gene-body methylation involves the exposure of intragenic regions to DNA methyltransferases, considering that RNA polymerase disrupts the chromatin structure during transcription. However, not all transcripts across gDMRs corresponded to highly expressed genes in oocytes (Figure 6C). Therefore, other epigenetic marks with an open chromatin structure might also be important for DNA methylation in oocytes. For instance, a recent knockout study showed that *Kdm1b*, which encodes histone H3K4 demethylase, is required for the establishment of some maternal methylation imprints [45]. Thus, several factors, including transcriptional and epigenetic modifica-

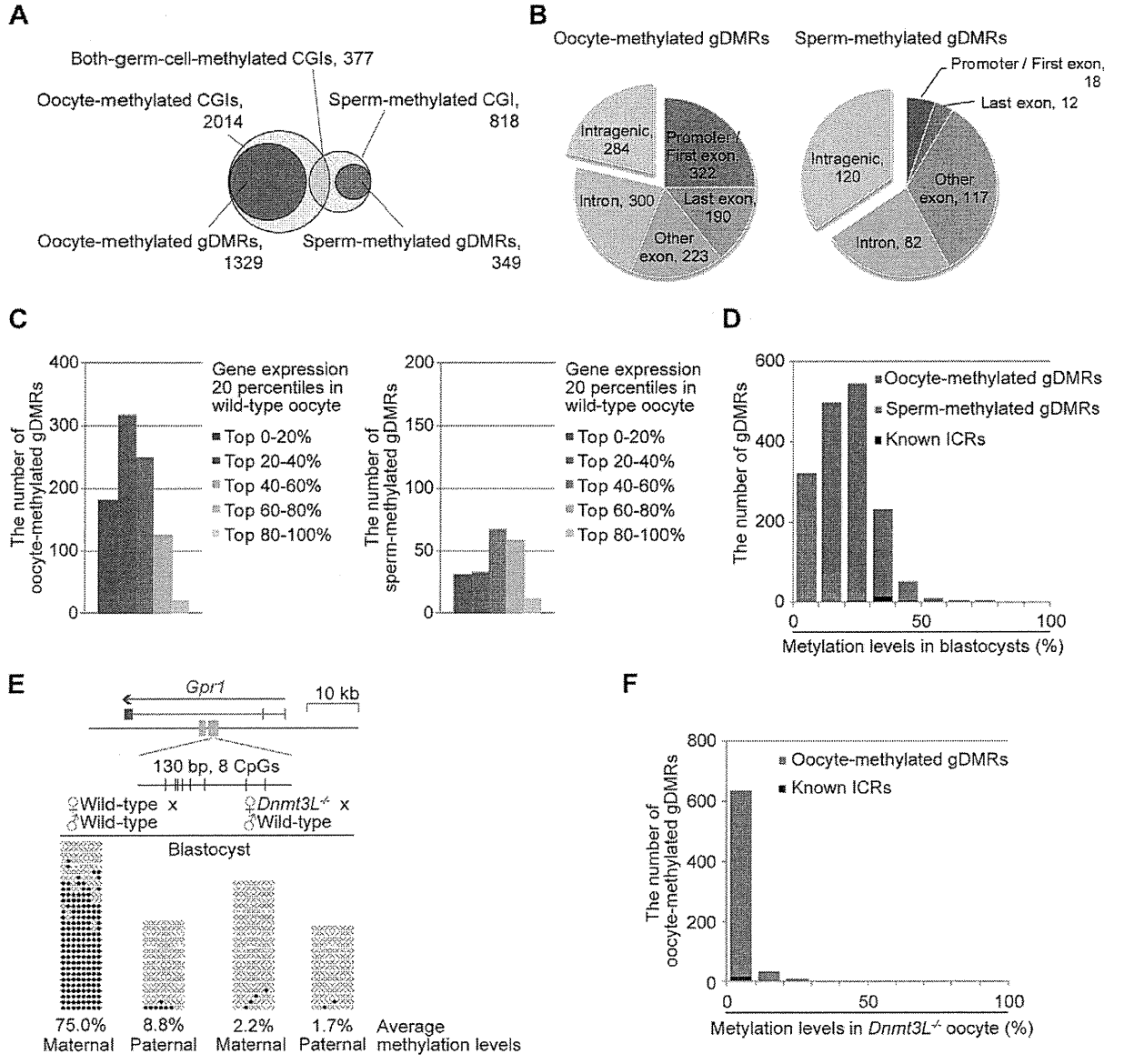

Figure 6. Identification of germline differentially methylated CGIs from DNA methylome profiles. (A) Venn-like diagram of two groups of CGIs, namely, oocyte-methylated CGIs (light pink) and sperm-methylated CGIs (light blue) and two groups of gDMRs, namely, oocyte-methylated gDMRs (red) and sperm-methylated gDMRs (blue). (B) The genomic distribution of 1329 oocyte-methylated (left) and 349 sperm-methylated gDMRs (right). The gDMRs were classified into 5 genomic locations; promoter (within 500-bp upstream from the first exon) or first exon, last exon, other exon, intron, and intergenic region. (C) The locations of the intragenic 1045 oocyte-methylated (left) and 229 sperm-methylated gDMRs (right). The gDMRs were classified into 5 gene group locations; the genes were divided into 5 percentile groups according to their expression levels in wild-type oocytes and sperm, as shown in Figure 3. (D) Histograms of the methylation levels of the gDMRs in blastocysts. The number of newly identified oocyte-specific, sperm-specific methylated gDMRs, and known ICRs are shown in black, red, and blue, respectively. (E) Bisulfite sequencing at the *Gpr1* gDMR in mouse blastocysts. (*Top*) Schematic representation of paternally-expressed *Gpr1*. The gene and gDMRs are shown in blue and green, respectively, and CpG sites are represented by vertical bars. (*Bottom*) Methylated and unmethylated CpGs are indicated by open and closed circles, respectively. The maternal and paternal alleles were distinguished by three polymorphisms between C57BL/6N and JF1 mice (G/A at 63,247,064; T/A at 63,247,072; and TA/AG at 63,247,089–63,247,090 on chromosome 1). (F) Histograms of the methylation levels of the demethylation-resistant oocyte-methylated gDMRs in *Dnmt3L*$^{-/-}$ oocytes. The number of newly identified oocyte-specific, sperm-specific methylated gDMRs, and known ICRs are shown in black, red, and blue, respectively.
doi:10.1371/journal.pgen.1002440.g006

tions, might be involved in *Dnmt3L*-mediated intragenic methylation.

The results of this study show that gene-body methylation was correlated to gene expression in sperm. However, the extent of that correlation is much less than in oocytes due to genome-wide hypermethylation, including in low-CpG-density regions. In male germline cells, global methylation acquisition begins during late embryonic development and before birth [3]. To more clearly

show this correlation, analysis of early-stage germ cells in fetal or neonatal animals might be required. Surprisingly, a positive correlation between mRNA expression and gene-body methylation was not observed in mouse ESCs. In addition, the accumulation of non-CpG methylation was not observed in mouse ESCs. These results contradict the results of another study, which showed that active transcription was associated with intragenic DNA methylation with non-CpG methylation in human ESCs [22,23]. This discrepancy might reflect the differences between human and mouse ESCs, the precise cell derivations or culture conditions [46,47]. However, further comparative studies on germ cell epigenomes from other species are required to further elucidate the functional role of epigenetic marking systems.

In this study, a large number of heritable oocyte-specific methylation marks were identified within a set of novel CpG islands [37]. The difference in the number of oocyte- and sperm-specific gDMRs reflects the fact that only 3 or 4 paternally-methylated imprinted loci were observed, as compared to approximately 20 maternally-methylated imprinted loci. The reason for the relative abundance of oocyte-specific methylated CGIs might be related to the intragenic methylation of CpG-rich regions, which are hypomethylated in sperm. The results show that most of the oocyte-specific marks are *Dnmt3L*-dependent, similar to results recently obtained by RRBS-based analysis [38]. However, whether all of these CpG-rich regions serve as imprinting methylation marks is unclear. For instance, although many genes with oocyte-specific methylation marks were identified (Figure 6B), the evidence that these genes were imprinted was lacking (*e.g.*, *Piwil1* and *Dnmt1*). These methylation marks might not be involved in the formation of a fertile oocyte but might play crucial roles in gene expression after fertilization. Furthermore, ESC methylomes showed that many gDMRs, especially sperm-specific gDMRs, acquired new methylation patterns after implantation. Methylation of these CGIs might control tissue-specific gene expression [48,49]. Partial alternation of imprinted methylation patterns in ESCs were observed in the present study, potentially caused by significant differences in the extent of the ICRs during embryo development [39]. A fuller understanding of epigenetic stability will require further methylome profiling during early embryogenesis and stem cell differentiation. The present study also identified a gDMR as a novel ICR candidate in the intron of the imprinted *Gpr1* gene. Thus, traditional promoter arrays may not identify all ICRs. However, further analyses are needed to determine which gDMRs, identified in the CpG methylome maps, are true ICRs at the imprinted *Gpr1-Zdbf2* locus [40,50].

mRNA-seq results showed that the expression levels of most genes in the wild-type and *Dnmt3L*$^{-/-}$ oocytes were similar. For instance, the expression level of almost all oocyte-specific genes, which regulate ovarian follicle formation, reproduction, and early development, were not significantly altered (Figure 5B and Table S1). These results are consistent with the findings of previous studies, which showed that *Dnmt3L*$^{-/-}$ female mice were capable of producing fertile oocytes (however, their offspring were not viable due to the lack of imprinting) [5,6]. Thus, regulation of oocyte-specific genes must be beyond the control of *Dnmt3L*-dependent cytosine methylation.

Although *Dnmt3L*$^{-/-}$ oocytes showed global hypomethylation at low to high CpG densities, some families of retrotransposons, such as LINEs and LTRs, were partially methylated at moderate to high CpG densities. Therefore, *Dnmt3L*-independent methylation might be involved in the silencing of retrotransposons and completion of oocyte meiosis. Previously, De La Fuente et al. [51] showed that *Hells* (also known as *Lsh*), which encodes a member of the sucrose non-fermenter 2 (SNF2) family of chromatin remodeling proteins, is required for DNA methylation of IAP and pericentromeric satellite repeats as well as repression of IAP retrotransposition in pachytene oocytes. Unfortunately, measurement of the methylation levels of satellite DNA, which is abundant in the pericentromeric regions, was not possible because these sequences were excluded from our analysis. However, a previous sequencing study showed that methylation levels of satellite DNA did not differ between the wild-type and *Dnmt3L*$^{-/-}$ oocytes [52]. Combined, these results suggest the presence of 2 types of oocyte methylation patterns: (i) *Dnmt3L*-mediated intragenic methylation that is essential for early embryogenesis and (ii) *Dnmt3L*-independent retroviral and pericentromeric methylation, which may be mediated by *Hells* activity, is crucial for oocyte meiosis [51]. Further studies on *Hells*-mediated oocyte methylation are required to elucidate the details of this mechanism.

Previous studies on the cytosine methylation of mtDNA have been highly controversial. A recent study by Shock et al. [53] reported cytosine methylation and hydroxymethylation in mammalian mitochondria. Our results indicated that mtDNA is unmethylated in blastocysts and ESCs, but is partially methylated in germ cells. Whether or not 5-hydroxymethylcytosine (5-hmC) exists in mitochondrial or genomic chromosomes of germ cells remains unclear. Meanwhile, rapid hydroxylation of 5-methylcytosine (5-mC) in the paternal pronucleus during zygotic development was also recently reported [54,55]. Currently, it is difficult to assess hydroxymethylation profiles in oocyte genomes due to the limited DNA recovery. Further investigation of cytosine modification during germ cell and zygote development will be required in the future to better understand this process.

The DNA methylome maps of mouse germ cells, in this study, were derived from SBS data and, therefore, accurately represent methylation levels of individual CpGs on a whole-genome level. The adaptation of the SBS method for small-scale DNA analysis, described in the present report, has the potential to enable further analyses of germline lineages. The current work examined SBS library construction using 3 methods, MethylC-seq, WBA-seq, and PBAT. MethylC-seq basically required only microograms of DNA [22,23,56], thus over amplification might cause redundancy in oocyte libraries. The latter methods allow comprehensive methylome analysis in samples with low amounts of starting DNA by avoiding DNA damage due to sodium bisulfite treatment (after adapter ligation, in the case of MethylC-Seq). Recent studies using BS sequencing have shown that methylated cytosine is abundant in the non-CpG regions of human pluripotent stem cells and mouse oocytes [22,23,39,56]; however, the function of non-CpG methylation in mammalian genomes remains unclear. The PBAT results also showed an abundance of non-CpG methylation in oocytes, with results similar to a previous sequencing study on imprinted loci [39]. However, accurate assessment of non-CpG methylation is required using increased sequencing depths because methylation levels of the non-CpG sites were much lower than those of the CpG sites. SBS library construction was conducted by WBA-seq from 2000 fully matured (metaphase II stage) oocytes; sufficient quantities for sequencing were not obtained. During oogenesis, most of the oocyte specific imprinted methylation marks were established during the GV stage. This contrasted to a previous study where a continuous increase in methylation levels was observed [38]. Further improvement of SBS methods, requiring smaller amounts of DNA, is needed to provide complete germ cell methylome maps and to elucidate the exact function of non-CpG methylation in germ cells.

In conclusion, we constructed the first extensive, high-resolution maps of DNA methylomes of mouse oocytes and sperm. These maps described the epigenetic properties of these DNA methylomes. Our data could serve as a platform for future studies to elucidate the role of epigenetic modifications in the development and functioning of germ and stem cells. Such studies are anticipated to improve our understanding of epigenetic reprogramming.

Materials and Methods

Preparation of MethylC-seq libraries

Five thousand germinal vesicle (GV)-stage oocytes were collected from the ovarian follicles of adult (7- to 9-week-old) female C57BL/6N mice (Clea Japan, Tokyo, Japan) 44–48 h after they were injected with equine chorionic gonadotropin. Three hundred blastocysts at embryonic day 3.5 were obtained from superovulated adult female C57BL/6N mice by flushing the uterus. Genomic DNA was extracted using the QIAamp DNA Mini Kit (Qiagen, Valencia, CA). Sperm were released from the cauda epididymises of adult male C57BL/6N mice. Sperm DNA was isolated by a standard phenol-chloroform extraction procedure with dithiothreitol (DTT). Genomic DNA from 2 lines of ESCs derived from C57BL/6J mice (Clea Japan) was extracted using the DNeasy Blood & Tissue Kit (Qiagen). DNA samples were sheared into 100-bp fragments in oocytes and 200-bp fragments in other samples using the Covaris S2 focused acoustic system (Covaris, Woburn, MA). Cytosine-methylated adapters (Illumina, San Diego, CA) were ligated to DNA by using the Paired-End DNA Sample Prep Kit or ChIP-Seq DNA Sample Prep Kit (Illumina). DNA fragments were isolated by 2–3% agarose gel electrophoresis and purified using the QIAquick Gel Extraction Kit (Qiagen). Sodium bisulfite conversion was performed using the Epitect Bisulfite Kit (Qiagen).

All bisulfite-converted DNA molecules were polymerase chain reaction (PCR)-amplified as follows: 2.5 U of Hot Start Taq polymerase (TaKaRa, Tokyo, Japan), 5 μL 10× PCR buffer, 25 μM dNTPs, 1 μL of each PCR Primer PE 1.0 and 2.0 (Illumina) (50 μL final). Thermocycling parameters were: initial denaturation at 94°C for 1 min, 15–25 cycles of denaturation at 94°C for 30 s, annealing at 65°C for 30 s, and extension at 72°C for 30 s, followed by a final extension at 72°C for 5 min. PCR reaction products were purified using the QIAquick kit (Qiagen).

Preparation of whole WBA-seq libraries

Two thousand GV-stage oocytes were collected from 7- to 9-week-old female C57BL/6N mice (Clea Japan) and, 2300 GV-stage oocytes were collected from 7–15-week-old *Dnmt3L*$^{-/-}$ female mice (129SvJae×C57BL/6N hybrid genetic background) [6,57]. Genomic DNA was extracted using the QIAamp DNA Mini Kit (Qiagen), and then bisulfite-treated with Epitect Bisulfite Kit (Qiagen). Subsequently, the bisulfite-converted DNA was amplified using Epitect Whole Bisulfitome Kit (Qiagen). The collected DNA was sheared into 200-bp fragments using Covaris S2. Unmodified Paired-End adapters (Illumina) were ligated to the DNA by using the Paired-End DNA Sample Prep Kit (Illumina). DNA fragments were isolated by 2% agarose gel electrophoresis and purified using the QIAquick Kit (Qiagen). All DNA was PCR amplified and purified in the same manner as the MethylC-seq method, except the number of PCR cycles was reduced to 7.

Preparation of PBAT libraries

GV-stage oocytes (400) and blastocysts (100) were obtained from 7- to 9-week-old female C57BL/6N mice (Clea Japan), and genomic DNA was extracted using the QIAamp DNA Mini Kit (Qiagen). The isolated oocyte and blastocyst genomic DNA and 100 ng of genomic DNA from sperm, blastocysts, and ESCs containing 1:200 amount of unmethylated lambda DNA (Invitrogen, Carlsbad, CA) were bisulfite-treated using the MethylCode Bisulfite Conversion Kit (Invitrogen). Details of the PBAT method are unpublished [Miura F & Ito T, personal communication]. Briefly, bisulfite-treated DNA were double-stranded using Klenow Fragments (3′- 5′ exo-) (New England Biolabs, Ipswich, MA) with random primers containing 5′ biotin tags and Illumina PE adaptors. The biotinylated molecules (first strand) were captured using Dynabeads M280 Streptavidin (Invitrogen) and double-stranded using Klenow Fragments (3′-5′ exo-) with random primers containing Illumina PE adaptors (second strand). Finally, template DNA strands were synthesized as complementary DNA with a second strand (unmethylated C is converted to T) using Phusion Hot Start High-Fidelity DNA Polymerase (New England Biolabs) with PCR Primer PE 1.0 (Illumina).

Preparation of mRNA sequencing libraries

Total RNA from 1000 wild-type GV oocytes, 500 *Dnmt3L*$^{-/-}$ GV oocytes, sperm, and ESCs was extracted using the RNeasy Mini Kit (Qiagen) and treated with DNase I (Promega, Madison, WI). RNA-Seq libraries were constructed using the mRNA-Seq Sample Preparation Kit (Illumina).

Sequencing

The MethylC-seq for blastocysts, WBA-seq, and PBAT libraries were sequenced on a HiSeq 2000 sequencing system (Illumina); the other MethylC-seq and mRNA-seq libraries were sequenced on a Genome Analyzer II (Illumina). Sample preparation, cluster generation, and sequencing were performed using the Paired-End Cluster Generation Kit-HS and the TruSeq SBS Kit-HS for the HiSeq 2000. Similarly, the Paired-End Cluster Generation Kits v2 and v4 and 18- and 36-Cycle Sequencing Kits v3 and v4 were used for the Genome Analyzer II. All kits were from Illumina.

Gene mapping

All sequenced reads were processed using the standard Illumina base-calling pipeline (v1.4–1.7). Generated sequence tags were mapped onto the mouse genome (mm9, UCSC Genome Browser, July 2007, Build 37.1) by using the Illumina ELAND program.

MethylC-seq tags (36 or 76 nt) were mapped with a custom Perl program, as described previously [17,22]. Briefly, all cytosines in the tags were replaced by thymines. Next, these tags were aligned to 2 mouse genome reference sequences (mm9), such that the antisense strand had cytosines replaced by thymines and the sense strand had guanines replaced by adenines. Finally, all tags (32–76 nt) that mapped uniquely without any mismatches to both strands were compiled and used for further analyses.

The 76 nt WBA-seq tags were mapped as follows. All tags were converted to 2 types of reads; in 1 read ("For" read), cytosines were replaced by thymines and in the other read ("Rev" read), guanines were replaced by adenines. Both "For" and "Rev" reads were aligned to sense and antisense mm9 strands. A total of 793, 397, 948, 480, and 238 million tags were aligned in wild-type oocytes, *Dnmt3L*$^{-/-}$ oocytes, sperm, blastocysts, and ESC genomes, respectively. To avoid bias, tags mapped with multiple hits or matched chromosome M (mitochondria), chromosome Y, or 3 types of repetitive sequences (simple repeat, low complexity repeat, and satellite DNA sequences) were omitted from further analyses.

The 47 nt PBAT tags (trimmed first 4 nt and last 1 nt) were mapped as follows. All guanidines in the tags were replaced by

adenines, and these tags were aligned to sense and antisense strands mm9.

For gene-level analysis, the concentrations of the perfectly matching 35 nt (trimmed first nt) mRNA-seq tags from wild-type oocytes, *Dnmt3L*$^{-/-}$ oocytes, sperm, and ESCs were calculated for the genomic regions corresponding to those covered by the RefSeq transcript models. The expression level of 20,854 unique genes was ranked by expression levels (calculated as RPKM values) in each library (Table S1). A total of 33, 28, 23, and 25 tags were aligned in 4 mRNA-seq libraries, respectively. mRNA-seq data analysis was performed and visualized using GenomeStudio Data Analysis software (Illumina).

Methylation analysis

The percentage of individual cytosines methylated at all CpG sites covered by at least 1 read was calculated as 100×(number of aligned cytosines (methylated cytosines))/(total number of aligned cytosines and thymines (originally unmethylated cytosines)). All genomic CpG methylation data are available on our website (http://www.nodai-genome.org/mouse_en.html). The CpG and non-CpG (CpH) methylation levels determined by PBAT results were calculated as the ratio between the total read C and the total read T mapped to genomic cytosines. Bisulfite conversion failure rates were calculated by read C:T ratios from lambda DNA mapping data. The failure rates were as follows: GV oocyte, 0.009; sperm, 0.008; blastocysts, 0.011; and ESCs, 0.006. Locations of transposable elements in the mouse genome (mm9) were obtained from the UCSC Genome Browser, and the average methylation levels of the whole genome and each transposable element were recalculated from the ratio of the aligned cytosines and thymines in each sequence. Lists of 23,021 CGIs were obtained from a previous report [37]. Around the TSS and TTS (±5 kb), genomic regions were divided into 20-bp bins. For each bin, the average methylation value was calculated for each gene. The expression level of 20,854 genes was divided into 5 percentile groups ranked by RPKM values, and the average methylation level for each group was mapped onto the gene structure model. These computational analyses were performed using a custom Perl program. Supercomputing resources were provided by the Human Genome Center, Institute of Medical Science, University of Tokyo.

Statistical analysis

Correlations between gene expression ranks and average methylation levels in the promoter (±500 bp from the TTS) or gene-body regions (gene-body 1: +2 to +5 kb from the TSS; gene-body 2: 0 to −5 kb from the TTS) were calculated using Spearman's rank correlation coefficient (ρ). An R-squared value (R^2) was calculated to evaluate the correlation of RPKM values between wild-type and *Dnmt3L*$^{-/-}$ oocytes. Statistical analysis was performed using the R statistical package.

Bisulfite sequencing

To analyze the methylation of the three transposable elements (L1 LINE, B1/Alu SINE, and IAP LTR), 20 wild-type GV oocytes were obtained from adult female C57BL/6N mice. Bisulfite sequencing conditions and primer sets for the three transposable elements were described, previously [52]. To analyze the methylation of the *Gpr1* locus, 10 blastocysts were obtained from BJF1 (C57BL/6N×JF1) and *Dnmt3L*$^{mat-/-}$ (*Dnmt3L*$^{-/-}$ ×JF1) mice [6,57]. Genomic DNA from blastocysts was isolated using the QIAamp DNA Mini Kit (Qiagen) and treated with sodium bisulfite with the Epitect Bisulfite Kit (Qiagen). The *Gpr1* gDMR sequence was amplified with 2 rounds of nested PCR. The first-round PCR reaction contained 1 U of Hot Start Taq polymerase (TaKaRa), 1× PCR buffer, 200 μM dNTPs, 1 μM forward primer, and 1 μM reverse primer (20 μL final). Thermocycling parameters were as follows: initial denaturation at 94°C for 1 min, 35 cycles of denaturation at 94°C for 30 s, annealing at 50°C for 30 s, and extension at 72°C for 30 s, followed by a final extension at 72°C for 5 min. Subsequently, 2 μL of the product was used as the input for the second-round PCR, which was performed in the same manner. Primer sets for the nested PCR were as follows: Gpr1-BSF1 (5′-GATTAGATTAGGTTAGTTTGGAA-3′) and Gpr1-BSR1 (5′-ACTAAAACACTAATCACCAAATA-3′) for the first round; Gpr1-BSF2 (5′-AGATTAGGTTAGTTTGGAATT-3′) and Gpr1-BSR2 (5′-AACACTAATCACCAAATAATTC-3′) for the second round. The second-round PCR product was subcloned and sequenced, as described previously [50]. The percentage methylation was calculated as 100×(number of methylated CpG dinucleotides)/(total number of CpGs). At least 10 clones from each parental allele were sequenced. Sequence data were analyzed using the QUMA quantification tool for methylation analysis [58].

Accession number

The MethylC-seq, WBA-seq, PBAT, and mRNA-seq data in this study have been deposited in the DNA Data Bank of Japan (DDBJ) under accession number DRA000484.

Supporting Information

Figure S1 Schematic of the SBS library construction procedure. MethylC-Seq libraries were generated by ligation of methylated sequencing adapters to fragmented genomic DNA followed by gel purification, sodium bisulfite conversion, and PCR amplification (*left*). WBA-seq libraries were generated by ligation of unmodified sequencing adapters to bisulfite-modified (amplified using EpiTect Whole Bisulfitome Kits) and fragmented genomic DNA followed by gel purification and PCR amplification (*middle*). PBAT libraries were generated by double-stranded DNA synthesis from bisulfite-treated (single-stranded) DNA with random primers containing sequencing adapters (*right*).
(TIF)

Figure S2 The percent of the oocyte and sperm genomes covered by differing minimum numbers of MethylC-seq and WBA-seq reads.
(TIF)

Figure S3 Sequencing bias towards mitochondrial and repetitive DNA sequences. (A) Average read depths for autosomal chromosomes and chromosome M (mitochondria) of mouse oocyte and sperm genomes. Occupancy of transposable elements in reads from SBS libraries before (B) and after (C) filtering the biased reads. (D) Genomic CpG coverage of SBS reads for each chromosome of mouse oocyte (orange: MethylC-seq, red: combined between MethylC-seq and WBA-seq) and sperm genomes (blue).
(TIF)

Figure S4 Average CpG methylation levels in genomic chromosomal DNA and mitochondrial DNA.
(TIF)

Figure S5 High-resolution DNA methylome map on mouse X inactivation center region in chromosome X (100,200,000–101,200,000). GenomeStudio view of Refseq's positions, repetitive element, CpG methylation map, CpG densities, CGI positions, and CGI methylation map were shown. Red, purple, blue, green,

and khaki dots and boxes represent the methylation levels at individual CpGs and CGIs in wild-type oocyte, *Dnmt3L*$^{-/-}$ oocyte, sperm, blastocyst, and ESC genomes, respectively, as shown in Figure 1.
(TIF)

Figure S6 DNA methylome maps of each chromosome of mouse germ cells. The methylation levels of each chromosome in wild-type oocytes, *Dnmt3L*$^{-/-}$ oocytes, and sperm in 10 kb windows (excluding mitochondrial chromosome, chromosome Y, and unplaced contigs). Red, purple, and blue lines represent the methylation levels in wild-type oocytes, *Dnmt3L*$^{-/-}$ oocytes, and sperm, respectively. Red and blue boxes represent oocyte-methylated and sperm-methylated gDMRs, and red and blue pins indicate maternal and maternal ICRs, respectively.
(TIF)

Figure S7 Methylation profiling of transposable elements in mouse germ cells. (A) CpG methylation levels are plotted as a function of CpG densities for L1 LINE, B1/Alu SINE, and LTR/ERVK retrotransposons (approximately 10% of the latter are intracisternal A particle (IAP) LTRs). Data for high CpG densities including less than 100 genomic CpGs were not plotted. (B) Bisulfite sequencing of L1 LINE, B1/Alu SINE, and IAP LTR retrotransposons. Methylated and unmethylated CpGs are indicated by open and closed circles, respectively.
(TIF)

Figure S8 Transcriptome and DNA methylome profiling at *H19-Igf2*, GenomeStudio view of mRNA-seq data (*top*) and CpG methylation map (*bottom*) of the genomic region spanning each locus. The blue shaded areas show the extent of the paternally-methylated gDMR.
(TIF)

Figure S9 Transcriptome and DNA methylome profiling at *Dnmt1*. The red shaded areas show the extent of the maternally-methylated gDMR.
(TIF)

Figure S10 Transcriptome and DNA methylome profiling at *Gpr1-Zdbf2*. The blue and red shaded areas show the extent of the paternally- and maternally-methylated gDMRs, respectively.
(TIF)

Figure S11 Quantification of the ratio of methylated (total number of read C) versus unmethylated cytosines (total number of read T) by PBAT results. Bar charts represent cytosine methylation ratio (A) at CpG (*left*), CpHpG (*middle*), and CpHpH (*right*) contexts and bisulfite-conversion failure rate (B) calculated by C:T ratio from lambda DNA mapping data. Total number of mapped reads is shown on these charts (*Top*).
(TIF)

Figure S12 Relationship between gene expression and intragenic methylation in ESCs. (A) The expression level of genes in ESCs was divided into 5 percentile groups. The distribution of methylation is shown ±5 kb from the transcription termination site (TTS; *left*) and transcription start site (TSS; *middle*). The graphs on the right show the average methylation levels in the promoter and gene-body regions. Spearman's rank correlation coefficient (ρ) was used to test the statistical significance of the correlation between gene expression and DNA methylation levels (*: $p<1\times10^{-9}$).
(TIF)

Figure S13 Expression profiles of DNA methyltransferase gene families. Red, purple, blue, and khaki bars represent RPKM values of individual genes in wild-type oocytes, *Dnmt3L*$^{-/-}$ oocytes, sperm, and ESCs.
(TIF)

Figure S14 Expression profiles of pluripotency-associated genes among wild-type oocytes, *Dnmt3L*$^{-/-}$ oocytes, sperm, and ESCs.
(TIF)

Figure S15 Histograms of the methylation levels of the demethylation-resistant (*left*) and demethylation-sensitive gDMRs (*right*) in ESCs. The number of oocyte-specific and sperm-specific methylated gDMRs is shown in red and blue, respectively.
(TIF)

Table S1 Gene transcript profiling for germ cells, blastocysts, and embryonic stem cells by mRNA-seq.
(XLSX)

Table S2 DNA methylation profiles of 23,021 CGIs.
(XLSX)

Table S3 Average DNA methylation profiles of 646 gDMRs determined by SBS and RRBS methods.
(XLSX)

Acknowledgments

We thank Terumi Horiuchi, Etsuko Sekimori, and Satoshi Sano for their assistance with analysis of the Illumina data. We are grateful to Fumihito Miura and Takashi Ito for their technical advice with the PBAT method and Takahiro Arima, Hitoshi Hiura, and Tom Moore for their helpful discussions and generous support.

Author Contributions

Conceived and designed the experiments: H Kobayashi, Y Suzuki, T Kono. Performed the experiments: H Kobayashi, T Sakurai. Analyzed the data: H Kobayashi, M Imai, Y Suzuki. Contributed reagents/materials/analysis tools: H Kobayashi, T Sakurai, M Imai, N Takahashi, A Fukuda, O Yayoi, S Sato, K Nakabayashi, K Hata, Y Sotomaru, Y Suzuki. Wrote the paper: H Kobayashi, T Kono.

References

1. Li E (2002) Chromatin modification and epigenetic reprogramming in mammalian development. Nat Rev Genet 3: 662–673.
2. Jaenisch R, Bird A (2003) Epigenetic regulation of gene expression: how the genome integrates intrinsic and environmental signals. Nat Genet 33 Suppl: 245–254.
3. Lees-Murdock DJ, Walsh CP (2008) DNA methylation reprogramming in the germ line. Epigenetics 3: 5–13.
4. Sasaki H, Matsui Y (2008) Epigenetic events in mammalian germ-cell development: reprogramming and beyond. Nat Rev Genet 9: 129–140.
5. Bourc'his D, Xu GL, Lin CS, Bollman B, Bestor TH (2001) Dnmt3L and the establishment of maternal genomic imprints. Science 294: 2536–2539.
6. Hata K, Okano M, Lei H, Li E (2002) Dnmt3L cooperates with the Dnmt3 family of de novo DNA methyltransferases to establish maternal imprints in mice. Development 129: 1983–1993.
7. Kaneda M, Okano M, Hata K, Sado T, Tsujimoto N, et al. (2004) Essential role for de novo DNA methyltransferase Dnmt3a in paternal and maternal imprinting. Nature 429: 900–903.
8. Kono T, Obata Y, Wu Q, Niwa K, Ono Y, et al. (2004) Birth of parthenogenetic mice that can develop to adulthood. Nature 428: 860–864.
9. Hirasawa R, Chiba H, Kaneda M, Tajima S, Li E, et al. (2008) Maternal and zygotic Dnmt1 are necessary and sufficient for the maintenance of DNA methylation imprints during preimplantation development. Genes Dev 22: 1607–1616.
10. Bourc'his D, Bestor TH (2004) Meiotic catastrophe and retrotransposon reactivation in male germ cells lacking Dnmt3L. Nature 431: 96–99.
11. Webster KE, O'Bryan MK, Fletcher S, Crewther PE, Aapola U, et al. (2005) Meiotic and epigenetic defects in Dnmt3L-knockout mouse spermatogenesis. Proc Natl Acad Sci U S A 102: 4068–4073.

12. Hata K, Kusumi M, Yokomine T, Li E, Sasaki H (2006) Meiotic and epigenetic aberrations in Dnmt3L-deficient male germ cells. Mol Reprod Dev 73: 116–122.
13. Shoji M, Tanaka T, Hosokawa M, Reuter M, Stark A, et al. (2009) The TDRD9-MIWI2 complex is essential for piRNA-mediated retrotransposon silencing in the mouse male germline. Dev Cell 17: 775–787.
14. Kuramochi-Miyagawa S, Watanabe T, Gotoh K, Takamatsu K, Chuma S, et al. (2010) MVH in piRNA processing and gene silencing of retrotransposons. Genes Dev 24: 887–892.
15. Cokus SJ, Feng S, Zhang X, Chen Z, Merriman B, et al. (2008) Shotgun bisulphite sequencing of the Arabidopsis genome reveals DNA methylation patterning. Nature 452: 215–219.
16. Down TA, Rakyan VK, Turner DJ, Flicek P, Li H, et al. (2008) A Bayesian deconvolution strategy for immunoprecipitation-based DNA methylome analysis. Nat Biotechnol 26: 779–785.
17. Lister R, O'Malley RC, Tonti-Filippini J, Gregory BD, Berry CC, et al. (2008) Highly integrated single-base resolution maps of the epigenome in Arabidopsis. Cell 133: 523–536.
18. Meissner A, Mikkelsen TS, Gu H, Wernig M, Hanna J, et al. (2008) Genome-scale DNA methylation maps of pluripotent and differentiated cells. Nature 454: 766–770.
19. Ball MP, Li JB, Gao Y, Lee JH, LeProust EM, et al. (2009) Targeted and genome-scale strategies reveal gene-body methylation signatures in human cells. Nat Biotechnol 27: 361–368.
20. Brunner AL, Johnson DS, Kim SW, Valouev A, Reddy TE, et al. (2009) Distinct DNA methylation patterns characterize differentiated human embryonic stem cells and developing human fetal liver. Genome Res 19: 1044–1056.
21. Deng J, Shoemaker R, Xie B, Gore A, LeProust EM, et al. (2009) Targeted bisulfite sequencing reveals changes in DNA methylation associated with nuclear reprogramming. Nat Biotechnol 27: 353–360.
22. Lister R, Pelizzola M, Dowen RH, Hawkins RD, Hon G, et al. (2009) Human DNA methylomes at base resolution show widespread epigenomic differences. Nature 462: 315–322.
23. Laurent L, Wong E, Li G, Huynh T, Tsirigos A, et al. (2010) Dynamic changes in the human methylome during differentiation. Genome Res 20: 320–331.
24. Popp C, Dean W, Feng S, Cokus SJ, Andrews S, et al. (2010) Genome-wide erasure of DNA methylation in mouse primordial germ cells is affected by AID deficiency. Nature 463: 1101–1105.
25. Serre D, Lee BH, Ting AH (2010) MBD-isolated Genome Sequencing provides a high-throughput and comprehensive survey of DNA methylation in the human genome. Nucleic Acids Res 38: 391–399.
26. Li Y, Zhu J, Tian G, Li N, Li Q, et al. (2010) The DNA methylome of human peripheral blood mononuclear cells. PLoS Biol 8: e1000533. doi:10.1371/journal.pbio.1000533.
27. Gu H, Bock C, Mikkelsen TS, Jager N, Smith ZD, et al. (2010) Genome-scale DNA methylation mapping of clinical samples at single-nucleotide resolution. Nat Methods 7: 133–136.
28. Howlett SK, Reik W (1991) Methylation levels of maternal and paternal genomes during preimplantation development. Development 113: 119–127.
29. Farthing CR, Ficz G, Ng RK, Chan CF, Andrews S, et al. (2008) Global mapping of DNA methylation in mouse promoters reveals epigenetic reprogramming of pluripotency genes. PLoS Genet 4: e1000116. doi:10.1371/journal.pgen.1000116.
30. Barhanin J, Lesage F, Guillemare E, Fink M, Lazdunski M, et al. (1996) K(V)LQT1 and lsK (minK) proteins associate to form the I(Ks) cardiac potassium current. Nature 384: 78–80.
31. Shin J, Bossenz M, Chung Y, Ma H, Byron M, et al. (2010) Maternal Rnf12/RLIM is required for imprinted X-chromosome inactivation in mice. Nature 467: 977–981.
32. Weber M, Hellmann I, Stadler MB, Ramos L, Paabo S, et al. (2007) Distribution, silencing potential and evolutionary impact of promoter DNA methylation in the human genome. Nat Genet 39: 457–466.
33. Edwards JR, O'Donnell AH, Rollins RA, Peckham HE, Lee C, et al. (2010) Chromatin and sequence features that define the fine and gross structure of genomic methylation patterns. Genome Res 20: 972–980.
34. Arnaud P, Hata K, Kaneda M, Li E, Sasaki H, et al. (2006) Stochastic imprinting in the progeny of Dnmt3L−/− females. Hum Mol Genet 15: 589–598.
35. Minami N, Tsukamoto S (2006) Role of oocyte-specific genes in the development of mammalian embryos. Reproductive Medicine and Biology 5: 175–182.
36. Chotalia M, Smallwood SA, Ruf N, Dawson C, Lucifero D, et al. (2009) Transcription is required for establishment of germline methylation marks at imprinted genes. Genes Dev 23: 105–117.
37. Illingworth RS, Gruenewald-Schneider U, Webb S, Kerr ARW, James KD, et al. (2010) Orphan CpG Islands Identify Numerous Conserved Promoters in the Mammalian Genome. PLoS Genet 6: e1001134. doi:10.1371/journal.ppat.1001134.
38. Smallwood SA, Tomizawa SI, Krueger F, Ruf N, Carli N, et al. (2011) Dynamic CpG island methylation landscape in oocytes and preimplantation embryos. Nat Genet 43: 811–814.
39. Tomizawa S, Kobayashi H, Watanabe T, Andrews S, Hata K, et al. (2011) Dynamic stage-specific changes in imprinted differentially methylated regions during early mammalian development and prevalence of non-CpG methylation in oocytes. Development 138: 811–820.
40. Hiura H, Sugawara A, Ogawa H, John RM, Miyauchi N, et al. (2010) A tripartite paternally methylated region within the Gpr1-Zdbf2 imprinted domain on mouse chromosome 1 identified by meDIP-on-chip. Nucleic Acids Res 38: 4929–4945.
41. Hellman A, Chess A (2007) Gene body-specific methylation on the active X chromosome. Science 315: 1141–1143.
42. Feng S, Cokus SJ, Zhang X, Chen PY, Bostick M, et al. (2010) Conservation and divergence of methylation patterning in plants and animals. Proc Natl Acad Sci U S A 107: 8689–8694.
43. Zemach A, McDaniel IE, Silva P, Zilberman D (2010) Genome-wide evolutionary analysis of eukaryotic DNA methylation. Science 328: 916–919.
44. Maunakea AK, Nagarajan RP, Bilenky M, Ballinger TJ, D'Souza C, et al. (2010) Conserved role of intragenic DNA methylation in regulating alternative promoters. Nature 466: 253–257.
45. Ciccone DN, Su H, Hevi S, Gay F, Lei H, et al. (2009) KDM1B is a histone H3K4 demethylase required to establish maternal genomic imprints. Nature 461: 415–418.
46. Ginis I, Luo Y, Miura T, Thies S, Brandenberger R, et al. (2004) Differences between human and mouse embryonic stem cells. Dev Biol 269: 360–380.
47. Tesar PJ, Chenoweth JG, Brook FA, Davies TJ, Evans EP, et al. (2007) New cell lines from mouse epiblast share defining features with human embryonic stem cells. Nature 448: 196–199.
48. Song F, Smith JF, Kimura MT, Morrow AD, Matsuyama T, et al. (2005) Association of tissue-specific differentially methylated regions (TDMs) with differential gene expression. Proc Natl Acad Sci U S A 102: 3336–3341.
49. Shiota K, Kogo Y, Ohgane J, Imamura T, Urano A, et al. (2002) Epigenetic marks by DNA methylation specific to stem, germ and somatic cells in mice. Genes Cells 7: 961–969.
50. Kobayashi H, Yamada K, Morita S, Hiura H, Fukuda A, et al. (2009) Identification of the mouse paternally expressed imprinted gene Zdbf2 on chromosome 1 and its imprinted human homolog ZDBF2 on chromosome 2. Genomics 93: 461–472.
51. De La Fuente R, Baumann C, Fan T, Schmidtmann A, Dobrinski I, et al. (2006) Lsh is required for meiotic chromosome synapsis and retrotransposon silencing in female germ cells. Nat Cell Biol 8: 1448–1454.
52. Kaneda M, Hirasawa R, Chiba H, Okano M, Li E, et al. (2010) Genetic evidence for Dnmt3a-dependent imprinting during oocyte growth obtained by conditional knockout with Zp3-Cre and complete exclusion of Dnmt3b by chimera formation. Genes to Cells 15: 169–179.
53. Shock LS, Thakkar PV, Peterson EJ, Moran RG, Taylor SM (2011) DNA methyltransferase 1, cytosine methylation, and cytosine hydroxymethylation in mammalian mitochondria. Proc Natl Acad Sci U S A 108: 3630–3635.
54. Iqbal K, Jin SG, Pfeifer GP, Szabo PE (2011) Reprogramming of the paternal genome upon fertilization involves genome-wide oxidation of 5-methylcytosine. Proc Natl Acad Sci U S A 108: 3642–3647.
55. Wossidlo M, Nakamura T, Lepikhov K, Marques CJ, Zakhartchenko V, et al. (2011) 5-Hydroxymethylcytosine in the mammalian zygote is linked with epigenetic reprogramming. Nat Commun 2: 241.
56. Lister R, Pelizzola M, Kida YS, Hawkins RD, Nery JR, et al. (2011) Hotspots of aberrant epigenomic reprogramming in human induced pluripotent stem cells. Nature 471: 68–73.
57. Koide T, Moriwaki K, Uchida K, Mita A, Sagai T, et al. (1998) A new inbred strain JF1 established from Japanese fancy mouse carrying the classic piebald allele. Mamm Genome 9: 15–19.
58. Kumaki Y, Oda M, Okano M (2008) QUMA: quantification tool for methylation analysis. Nucleic Acids Res 36: W170–175.

Depletion of Invariant NKT Cells Reduces Inflammation-Induced Preterm Delivery in Mice

Li-Ping Li,* Yi-Chuan Fang,* Guo-Fa Dong,* Yi Lin,† and Shigeru Saito‡

This study sought to determine whether invariant NKT (iNKT) cells play an essential role in inflammation-induced preterm delivery. Preterm delivery and fetal death rates were determined in wild-type (WT) C57BL/6 mice and iNKT cell-deficient Jα18$^{-/-}$ mice injected i.p. with LPS. The percentages of decidual immune cells, including activated subsets, and costimulatory molecule expression were analyzed by flow cytometry. Th1 and Th2 cytokine production in the culture supernatants of decidual mononuclear cells was measured by ELISA. To some extent, Jα18$^{-/-}$ mice were resistant to LPS-induced preterm delivery. The proportions of decidual CD3$^+$ and CD49b$^+$ cells were slightly lower in Jα18$^{-/-}$ mice than in WT Jα18$^{+/+}$ mice, whereas almost no CD3$^+$CD49b$^+$ cells could be found in Jα18-null mice. The percentages of activated decidual DCs, T cells, and NK cells were significantly lower in LPS-treated Jα18$^{-/-}$ mice than in WT mice. The CD40, CD80, and CD86 expression levels on decidual CD11c$^+$ cells from Jα18$^{-/-}$ mice were also significantly lower than in WT mice. Mean concentrations of Th1 cytokines IFN-γ and IL-12p70 in the culture supernatants of decidual mononuclear cells from LPS-treated Jα18$^{-/-}$ mice were apparently lower than those of LPS-induced WT mice. Additionally, the proportions of activated CD11c$^+$ cells, CD3$^+$ cells, and CD49b$^+$ cells in LPS-induced preterm delivery mice were strikingly higher in both WT and null mice when compared with the control PBS group and LPS-injected but normally delivered mice. Our results suggest that iNKT cells may play an essential role in inflammation-induced preterm birth. *The Journal of Immunology*, **2012, 188: 4681–4689.**

Preterm birth, defined as childbirth occurring at <37 completed weeks or 259 d gestation, occurs in 9.6% of all births worldwide (1). Preterm birth is recognized as a worldwide problem, accounting for >80% of neonatal deaths and >50% of long-term morbidity in the surviving infants (2). Among surviving infants, preterm birth is implicated by long-term neurodevelopmental disabilities, mental retardation, and cognitive, executive, and educational deficits (3–5).

The most common cause of preterm birth is infection, which is largely subclinical in nature (6). Up to 30% of cases of spontaneous preterm birth are associated with intrauterine microbial colonization or histological evidence of chorioamnionitis. Intraamniotic inflammation is found in approximately half of the cases of preterm labor and premature preterm rupture of membranes (7). The presence of intrauterine inflammation is not only a cause of preterm birth but is also associated with an increase in neonatal morbidity and mortality.

TLRs are a group of pattern-recognition receptors that recognize conserved microbial structures called pathogen-associated molecular patterns on the surface of bacteria, viruses, fungi, and protozoans. TLRs play an essential role in immune recognition, cell signal transduction, upstream events of immune response cascades, and inflammation-induced preterm birth (8–10). Despite a growing association between TLRs and inflammation-induced preterm birth, the precise mechanisms of TLR-mediated inflammation at the maternal/fetal interface are largely unknown.

NKT cells are a subset of innate lymphocytes that were originally identified as an unusual T cell population that coexpress TCRs and receptors of the NK cell lineage. Most NKT cells express a semi-invariant TCR, Vα14-Jα18/Vβ8.2, Vβ7, or Vβ2 in mice and Vα24-Jα18/Vβ11 in humans (11). As such, these cells have a limited ligand repertoire and are referred to as invariant NKT (iNKT) cells or type I NKT cells. In sharp contrast with conventional T cells, which recognize peptide Ags presented by MHC class I or II proteins, iNKT cells are specific for glycolipid Ags presented by the MHC class I-related protein CD1d (12).

NKT cells are different from functionally differentiated conventional αβ T cells in that they are autoreactive and swiftly produce copious amounts of both Th1 and Th2 cytokines, including IL-4, IL-10, and IFN-γ, upon stimulation with their ligands (12). The cytokines secreted by activated iNKT cells amplify the immune response initiated by these cells through transactivation of other cell types, including conventional CD4 and CD8 T cells, dendritic cells (DCs), NK cells, B cells, regulatory T cells, macrophages, and neutrophils (11), and they influence a broad spectrum of immunological responses, including autoimmunity (13), antimicrobial host responses (14), resistance to tumors (15), and transplantation immunity (16).

It is reported that activation of human APCs by TLR ligands modulates the lipid biosynthetic pathway, resulting in enhanced recognition of CD1d-associated lipids by iNKT cells, as defined by

*Department of Obstetrics and Gynecology, Guangzhou Medical College Affiliated Guangzhou First Municipal People's Hospital, Guangzhou 510180, China; †Department of Obstetrics and Gynecology, Renji Hospital, School of Medicine, Shanghai Jiaotong University, Shanghai 200127 China; and ‡Department of Obstetrics and Gynecology, Faculty of Medicine, University of Toyama, Toyama 930-0194, Japan

Received for publication September 19, 2011. Accepted for publication March 5, 2012.

This work was supported by the Guangdong Natural Science Fund (7301628), the Guangdong Medical and Scientific Research Fund (A2008512), Guangzhou Medical Science and Technology Projects (20121A011020), the National Funds for Distinguished Young Scientists, China (81125004), and by a grant from the Ministry of Education, Culture, Sports, Science and Technology, Japan [Grant-in-Aid for Scientific Research (B)-23390386].

Address correspondence and reprint requests to Dr. Yi Lin or Dr. Shigeru Saito, Department of Obstetrics and Gynecology, Renji Hospital, School of Medicine, Shanghai Jiaotong University, Shanghai, 200001, China (Y.L.) or Department of Obstetrics and Gynecology, Faculty of Medicine, University of Toyama, Toyama 930-0194, Japan (S.S.). E-mail addresses: yilinonline@gmail.com (Y.L.) and s30saito@med.u-toyama.ac.jp (S.S.)

Abbreviations used in this article: DC, dendritic cell; iNKT cell, invariant NKT cell; WT, wild-type.

www.jimmunol.org/cgi/doi/10.4049/jimmunol.1102628

IFN-γ secretion (17). APC-derived soluble factors further increase CD1d-restricted iNKT cell activation (17). Therefore, iNKT cells at the maternal/fetal interface may be activated by self-lipid Ags versus soluble factors from DCs upon TLR signaling, and play a role in inflammation-induced preterm birth. As we have previously demonstrated that TLR4 plays an important role in LPS-induced preterm birth (18), we wanted to assess in this study the impact of iNKT cells on TLR4-induced inflammatory preterm birth.

Conventional T cells do not express the invariant Vα14-Jα18 Ag receptor (19), indicating their selective usage in Vα14 NKT cells. Thus, disruption of the invariant Vα14-Jα18 receptor results in the selective loss of Vα14 NKT cells, leaving other types of lymphoid cells intact, including T, B, and NK cells (20, 21). $J\alpha18^{-/-}$ mice were found to be fertile and are healthy in appearance (22). The number of total lymphocytes in $J\alpha18^{-/-}$ mice are not significantly different from $J\alpha18^{+/+}$ mice, with the exception of a complete loss of Vα14 NKT cells (20, 21). Ito et al. (21) have described the possible role of decidual Vα14 NKT cells in the pathogenesis of abortion. However, it remains unclear whether iNKT cells play a key role in the pathogenesis of preterm labor. In our present study, we made use of $J\alpha18^{-/-}$ mice to investigate the possible role that iNKT cells may play in inflammation-induced preterm birth.

Materials and Methods

Animals

Eight-week-old female and male wild-type (WT) C57BL/6 mice and iNKT cell-deficient $J\alpha18^{-/-}$ mice on a C57BL/6 background were purchased from The Jackson Laboratory and subsequently maintained under pathogen-free conditions in the Laboratory Animal Facility of Guangzhou Medical College. Animals were acclimated in our facility for at least 2 wk before use in these experiments. All animal procedures followed the guidelines of the Chinese Council for Animal Care. Each female mouse was co-caged with one male. The point at which a vaginal plug was detected was designated as day 0 gestation.

LPS-induced preterm delivery model

As described previously (18), on day 15 gestation, the pregnant $J\alpha18^{-/-}$ mice or C57BL/6 mice were injected i.p. with 200 μl LPS (Sigma-Aldrich) saline solution with care not to enter the amniotic cavity. The dose of LPS was generally 50 μg/kg body weight, unless otherwise indicated. Pregnant WT mice and $J\alpha18^{-/-}$ mice injected i.p. with 200 μl PBS served as negative controls. Animals were observed closely for any signs of morbidity (piloerection, decreased movement, vaginal bleeding, and preterm delivery). Mice that delivered prematurely or delivered at term were autopsied when fetuses were found in the cage. Preterm delivery was defined as the finding of at least one pup in the cage or the lower vagina before gestation day 18 (not including gestation day 18). Fetal death was identified by white discoloration, markedly smaller fetal size, and lack of blood flow in the umbilical cord. The incidences of preterm delivery and fetal death were calculated. Preterm delivery rate was determined by total prematurely delivered mice/total pregnant mice. Fetal death rate was determined by total dead fetuses/total fetuses. Because the maternal mice may cannibalize dead pups before being counted, the fetal death rate may be underestimated. To minimize this possibility, mice were monitored frequently after PBS or LPS injection (no less than four times a day at an interval of <8 h).

Isolation of peripheral blood and decidual mononuclear cells

Peripheral blood samples were collected from the vena orbitalis, heparinized, and purified by centrifugation on Ficoll-Hypaque density medium (23). For decidual tissue harvest, the uterine horns of pregnant mice were opened longitudinally, and the whole placental and decidual unit was separated individually from the respective embryo and its implantation site. After washing in cold PBS, pooled decidual tissues were cut into small pieces (1 mm^3). To minimize the underestimation of immunological changes, samples from mice that gave live births or appeared healthy during gestation were separated from those with adverse outcomes in the same group. Only the samples from those with adverse outcomes in the same group were pooled, analyzed, and compared with the control group, unless otherwise indicated. The selected tissue was digested three times with 1 mg/ml Dispase II (Roche) at 37°C for 20 min in each cycle in a shaking water bath. When single or clumps of cells were observed under a microscope, the released cells were separated from undigested tissue pieces by filtering through a 50-μm-pore nylon mesh. Mononuclear cells were purified with Ficoll-Hypaque density medium (density, 1.077 ± 0.002 g/ml) by centrifugation at 800 × *g* for 20 min at 22°C. Any contaminating RBCs that might have persisted in peripheral blood or decidual single-cell suspension were eliminated by incubation with red cell lysis buffer (GenMed) (23).

Flow cytometry analysis

Every 10^6 PBMCs or decidual mononuclear cells in 50 μl PBS were incubated with PE/Cy5-conjugated CD45 (0.25 μg), PE-conjugated CD11c (0.25 μg), FITC-conjugated CD3 (0.5 μg), allophycocyanin/Cy7-conjugated CD19 (0.5 μg), allophycocyanin-conjugated CD49b (0.5 μg), and PE/Cy7-conjugated CD69 (0.25 μg) for 30 min at 4°C. In some cases, every 10^6 decidual mononuclear cells in 50 μl PBS were incubated with PE/Cy5-conjugated CD45 (0.25 μg), PE-conjugated CD11c (0.25 μg), FITC-conjugated CD40 (0.5 μg), allophycocyanin-conjugated CD80 (0.5 μg), and PE/Cy7-conjugated CD86 (0.5 μg) for 30 min at 4°C. After washing twice with PBS, cells were fixed in 10 g/l paraformaldehyde. Immunostained cells were analyzed on a FACSCanto flow cytometer using FACSDiva software (Becton Dickinson). Ten thousand cells were detected in each sample. Isotype controls were established using matched fluorescence-labeled isotype control Abs to avoid nonspecific staining. All of the fluorescence-labeled Abs and isotype controls were purchased from BioLegend.

The percentage of decidual $CD11c^+$ cells in the $CD45^+$ cell population was calculated as follows: % $CD11c^+$ cells in $CD45^+$ cell population = ($CD11c^+CD45^+$ cell number/$CD45^+$ cell number) × 100. In the same way, the percentages of decidual $CD3^+$ cells in the $CD45^+$ cell population, $CD19^+$ cells in the $CD45^+$ cell population, $CD49b^+$ cells in the $CD45^+$ cell population, $CD11c^+CD69^+$ cells in the $CD11c^+$ cell population, $CD3^+CD69^+$ cells in the $CD3^+$ cell population, $CD19^+CD69^+$ cells in the $CD19^+$ cell population, and $CD49b^+CD69^+$ cells in the $CD49b^+$ cell population were calculated. In other cases, the percentages of decidual $CD11c^+CD40^+$ cells in the $CD11c^+$ cell population, $CD11c^+CD80^+$ cells in the $CD11c^+$ cell population, and $CD11c^+CD86^+$ cells in the $CD11c^+$ cell population were calculated in the same way.

Decidual mononuclear cells harvested on gestation day 15 were isolated by density centrifugation and further purified using MACS microbead-conjugated anti-mouse CD3 and anti-mouse CD49b (Miltenyi Biotec) to obtain the indicated cell subsets. Cells were counted using a hemocytometer and compared between untreated $J\alpha18^{+/+}$ and $J\alpha18^{-/-}$ mice. The experiments were performed independently four times.

Cytokine assays

Decidual mononuclear cells were cultured in a 5% CO_2 atmosphere. After 24 h, culture supernatants were collected and stored at −80°C for cytokine examination. The levels of mouse cytokines, including IFN-γ, IL-12p70, IL-4, and IL-10, were assessed using commercially available ELISA kits from BD Pharmingen. All assays were conducted according to the manufacturer's instructions.

Statistical analysis

Preterm delivery rates were examined using a Fisher exact test, and fetal death rates were analyzed using the Pearson χ^2 text. Gestation length, cell percentages, and cytokine concentrations were determined by one-way ANOVA. Results were given as means ± SD. A p value of <0.05 was considered significant between analyzed groups.

Results

Comparison of gestation length between pregnant $J\alpha18^{+/+}$ mice and $J\alpha18^{-/-}$ mice

C57BL/6 mice normally deliver pups from day 19 to 21 of gestation. To determine whether iNKT cell deficiency influences the gestation length of normal labor, gestation lengths for PBS-treated $J\alpha18^{+/+}$ and PBS-treated $J\alpha18^{-/-}$ mice were compared. As shown in Fig. 1, the mean gestation length for iNKT cell-deficient $J\alpha18^{-/-}$ mice treated with PBS was 19.8 ± 0.8 d, which was not significantly different from that for $J\alpha18^{+/+}$ mice (20.0 ± 0.7 d). No

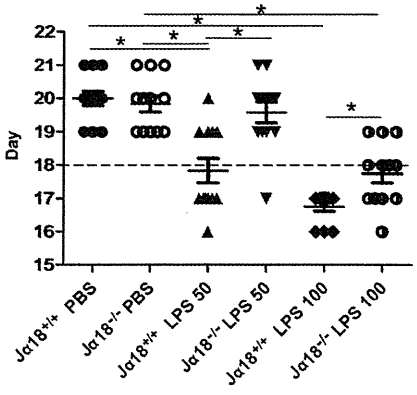

FIGURE 1. Comparison of gestation lengths between $J\alpha18^{+/+}$ and $J\alpha18^{-/-}$ mice. $J\alpha18^{+/+}$ and $J\alpha18^{-/-}$ mice were treated with PBS, or LPS at a dosage of 50 μg/kg body weight (LPS 50), or LPS at a dosage of 100 μg/kg body weight (LPS 100). *$p < 0.01$. Each spot below the dashed line indicates one preterm labor mouse.

labor delay was found in $J\alpha18^{-/-}$ mice. In comparison, the mean gestation length was significantly shorter in LPS-treated WT ($J\alpha18^{+/+}$) mice at a dosage of 50 μg/kg body weight than $J\alpha18^{-/-}$ mice with the same treatment (17.8 ± 1.3 versus 19.6 ± 1.1 d; $p = 0.001$). When the mice were treated with LPS at a dosage of 100 μg/kg body weight, a significantly decreased gestation length was observed in both WT and $J\alpha18^{-/-}$ mice (16.8 ± 0.5 versus 17.8 ± 1.0 d; $p = 0.004$). Thus, the LPS dosage of 50 μg/kg body weight was generally used in the present study (Fig. 1).

Comparison of preterm delivery rate and mortality

To access the intrinsic role of iNKT cells in inflammation-induced preterm delivery, the LPS-induced preterm delivery model was established in $J\alpha18^{+/+}$ mice and $J\alpha18^{-/-}$ mice, and the rates of preterm delivery and mortality were analyzed. In our model, i.p. injection of LPS at 50 μg/kg body weight resulted in a 58.3% preterm birth rate in $J\alpha18^{+/+}$ mice within 72 h, which was markedly higher than that of PBS-treated WT mice and PBS-treated $J\alpha18^{-/-}$ mice whose preterm birth rates were both zero ($p < 0.01$). All preterm delivered maternal mice delivered nonviable pups, and no maternal mortality or morbidity was observed. The incidence of preterm birth was significantly decreased in LPS-injected $J\alpha18^{-/-}$ mice (group D) compared with LPS-injected $J\alpha18^{+/+}$ mice (group C) ($p < 0.05$) (Table I).

Although the LPS dose of 100 μg/kg body weight caused a 100% preterm birth rate in WT mice, we still did not observe maternal mortality in this model. The incidence of preterm labor was markedly downregulated in LPS-treated $J\alpha18^{-/-}$ mice (group F) compared with LPS-treated $J\alpha18^{+/+}$ mice (group E) ($p < 0.01$), although it was still significantly higher than that of PBS-treated $J\alpha18^{+/+}$ mice (group A) ($p < 0.05$) or $J\alpha18^{-/-}$ mice (group B) ($p < 0.05$) (Table I).

In LPS-treated WT mice at a dosage of 50 μg/kg body weight, intrauterine demise was observed in 57.6% of fetuses, which was significantly higher than that found in PBS-treated $J\alpha18^{+/+}$ mice and PBS-treated $J\alpha18^{-/-}$ mice (fetal death rate of 3.0 and 3.8%, respectively; $p < 0.01$). Meanwhile, the mortality in LPS-treated $J\alpha18^{-/-}$ mice was markedly lower than in LPS-treated $J\alpha18^{+/+}$ mice ($p < 0.01$) (Table I).

A higher dosage of LPS (100 μg/kg) resulted in a 100% fetal death in WT mice. The incidence of fetal death was markedly lower in LPS-treated $J\alpha18^{-/-}$ mice (group F) than in LPS-treated $J\alpha18^{+/+}$ mice (group E) ($p < 0.01$), although it was still significantly higher than in PBS-injected $J\alpha18^{+/+}$ and $J\alpha18^{-/-}$ mice ($p < 0.01$ for both) (Table I). It is notable that the extent of fetal death reported in this study is probably inaccurate and likely to be underestimated, as the mother mice commonly cannibalize dead pups.

Comparison of the percentages of peripheral blood and decidual DC, T cell, B cell, and NK cell populations

To explore the mechanism underlying the decreased preterm delivery and fetal death rates in iNKT cell-deficient $J\alpha18^{-/-}$ mice, we examined the percentages of decidual DCs, T cells, B cells, and NK cells by detecting their respective surface markers CD11c, CD3, CD19, and CD49b. We found no significant difference in the percentages of decidual DCs and B cells between PBS-treated $J\alpha18^{+/+}$ and $J\alpha18^{-/-}$ mice. However, the percentages of decidual $CD3^+$ cells and $CD49b^+$ cells were slightly higher in $J\alpha18^{+/+}$ mice than in $J\alpha18^{-/-}$ mice. The percentages of decidual $CD3^+$ cells and $CD49b^+$ cells from LPS-injected $J\alpha18^{+/+}$ mice were significantly higher than those from PBS-injected $J\alpha18^{+/+}$ mice and $J\alpha18^{-/-}$ mice. Additionally, the percentages of decidual T cells and NK cells from LPS-injected $J\alpha18^{-/-}$ mice were markedly lower than those for LPS-treated $J\alpha18^{+/+}$ mice. Moreover, in peripheral blood from nonpregnant and pregnant mice, the numbers of DCs, T cells, B cells, and NK cells were similar among the four groups (Fig. 2).

Table I. Comparison of preterm delivery and mortality rates

Group	Mice	LPS	*n*	Preterm Delivery Rate	Mortality
A	$J\alpha18^{+/+}$	PBS	12	0 (0/12)	3.0% (3/101)
B	$J\alpha18^{-/-}$	PBS	12	0 (0/12)	3.8% (4/105)
C	$J\alpha18^{+/+}$	50 μg/kg	12	58.3% (7/12)[a,b]	57.6% (57/99)[a,b]
D	$J\alpha18^{-/-}$	50 μg/kg	12	8.3% (1/12)[c]	8.8% (9/102)[d]
E	$J\alpha18^{+/+}$	100 μg/kg	12	100% (12/12)[a,b]	100% (104/104)[a,b]
F	$J\alpha18^{-/-}$	100 μg/kg	12	41.7% (5/12)[e,f,g]	38.3% (41/107)[a,b,g]

On day 15 gestation, pregnant $J\alpha18^{-/-}$ and C57BL/6 mice were i.p. injected with 200 μl PBS or LPS at 50 or 100 μg/kg body weight. Mice that delivered preterm or delivered at term were autopsied when fetuses were found in the cage. The incidences of preterm delivery and fetal death were calculated. Preterm delivery rate = total preterm delivered mice/total pregnant mice. Fetal death rate = total dead fetuses/total fetuses.

[a] $p < 0.01$ versus group A.
[b] $p < 0.01$ versus group B.
[c] $p < 0.05$ versus group C.
[d] $p < 0.01$ versus group C.
[e] $p < 0.05$ versus group A.
[f] $p < 0.05$ versus group B.
[g] $p < 0.01$ versus group E.

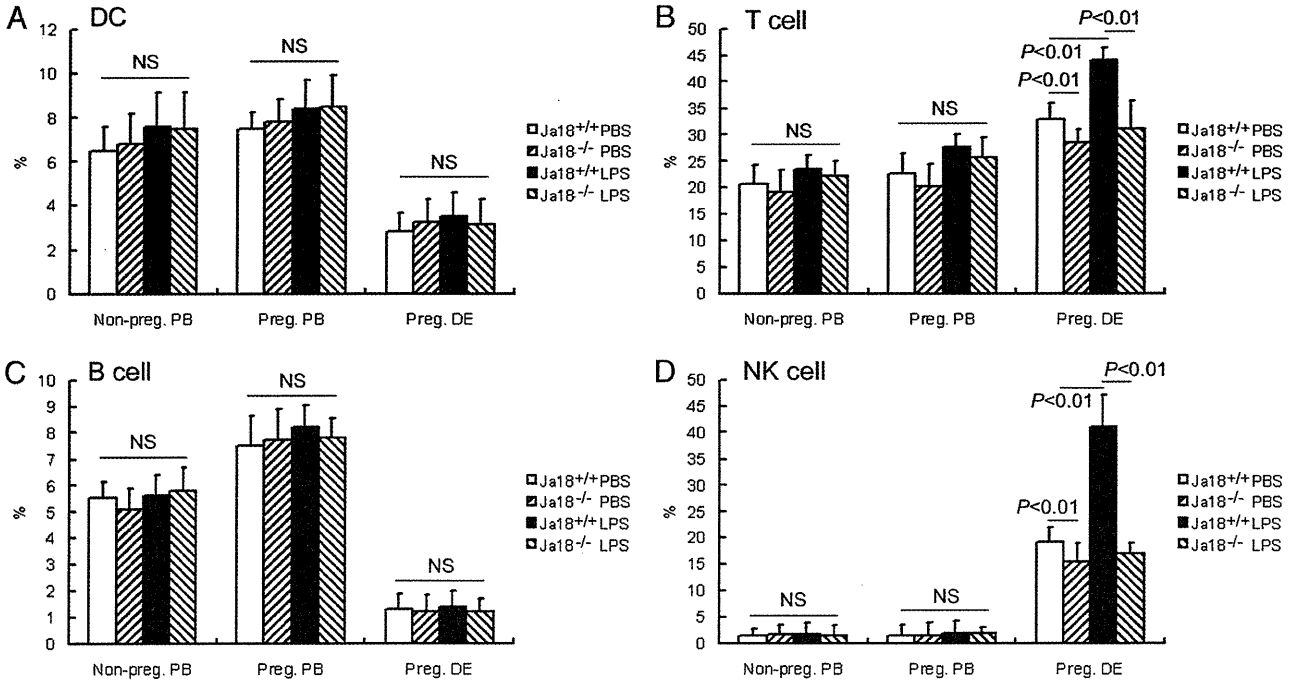

FIGURE 2. Percentages of peripheral blood and decidual DC (**A**), T cell (**B**), B cell (**C**), and NK cell (**D**) populations in nonpregnant and pregnant mice. Pregnant (Preg.) Jα18$^{-/-}$ mice or Jα18$^{+/+}$ mice were injected i.p. with PBS or LPS at 50 μg/kg body weight. PBMCs from nonpregnant mice and peripheral blood and decidual mononuclear cells from pregnant mice were isolated and incubated with fluorescence-conjugated anti-CD45, anti-CD11c, anti-CD3, anti-CD19, and anti-49b mAbs and isotype controls. The percentages of CD11c$^+$ cells, CD3$^+$ cells, CD19$^+$ cells, and CD49b$^+$ cells in the CD45$^+$ cells were calculated. Values represent means ± SD (n = 4 for each group).

Comparison of the absolute number of decidual CD3$^+$, CD49b$^+$, CD3$^+$CD49b$^-$, CD49b$^+$CD3$^-$, and CD3$^+$CD49b$^+$ cells

Absolute numbers of MACS-purified decidual CD3$^+$, CD49b$^+$, CD3$^+$CD49b$^-$, CD49b$^+$CD3$^-$, and CD3$^+$CD49b$^+$ cells were compared between untreated Jα18$^{+/+}$ mice and Jα18$^{-/-}$ mice, and the representative flow cytometry results are shown in Fig. 3A. Whereas almost no CD3$^+$CD49b$^+$ cells were found in Jα18$^{-/-}$ mice (0.8×10^4), a considerable number of the double-positive cells were observed in Jα18$^{+/+}$ mice (9.0×10^4; $p < 0.01$) (Fig. 3B). Both CD3$^+$ and CD49b$^+$ cell numbers were slightly higher in

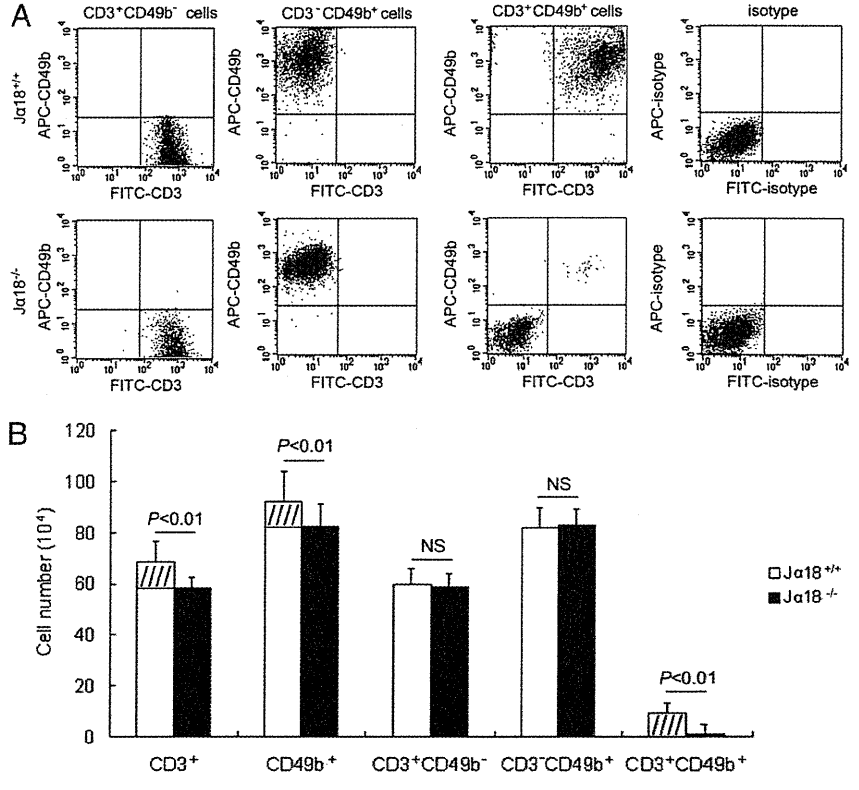

FIGURE 3. Comparison of the absolute number of decidual cell subsets between Jα18$^{+/+}$ and Jα18$^{-/-}$ mice. MACS-purified cell subsets were compared. (**A**) MACS-purified cells analyzed by flow cytometry. Cell purity routinely exceeded 97%. (**B**) Comparison of absolute cell numbers of indicated cell subsets. Results are shown as means ± SD (n = 4 for each group). Values of the shadowed bars are similar between the three indicated groups.

WT mice than in Jα18$^{-/-}$ mice (1.2-fold for CD3$^+$ cells and 1.1-fold for CD49b$^+$ cells; $p < 0.01$ for both), but no significant difference was found in the number of CD3$^+$CD49b$^-$ or CD49b$^+$ CD3$^-$ cells between Jα18$^{+/+}$ and Jα18$^{-/-}$ mice. In the WT mice the number of CD3$^+$CD49b$^-$ cells plus the number of CD3$^+$ CD49b$^+$ cells appeared approximately equal to the number of CD3$^+$ cells, and the number of CD49b$^+$CD3$^-$ cells plus the number of CD3$^+$CD49b$^+$ cells appeared approximately equal to the number of CD49b$^+$ cells, suggesting that the decreased decidual CD3$^+$ and CD49b$^+$ cell numbers in the Jα18$^{-/-}$ mice may be completely attributed to the absence of iNKT cells (Fig. 3B).

Comparison of the percentages of activated decidual DC, T cell, B cell, and NK cell populations

We also wanted to determine whether iNKT cells affect lymphocyte activation at the maternal/fetal interface. The early activation marker CD69 on decidual DCs, T cells, B cells, and NK cells were analyzed by flow cytometry. There was no statistically supported difference in the percentages of decidual activated DCs, T cells, B cells, or NK cells between PBS-treated Jα18$^{+/+}$ mice and PBS-treated Jα18$^{-/-}$ mice. At the dose of 50 μg/kg body weight, LPS-injected Jα18$^{+/+}$ mice showed markedly increased percentages of decidual activated DCs, T cells, and NK cells in comparison with PBS-injected Jα18$^{+/+}$ or Jα18$^{-/-}$ mice. The percentages of decidual activated DCs, T cells, and NK cells from LPS-injected Jα18$^{-/-}$ mice were strikingly reduced when compared with those from LPS-injected Jα18$^{+/+}$ mice.

At the dose of 100 μg/kg body weight, LPS-injected WT mice showed significantly increased percentages of decidual activated DCs, T cells, and NK cells in comparison with LPS-infused WT mice at the dose of 50 μg/kg. At the dose of 100 μg/kg, the percentages of activated decidual DCs, T cells, and NK cells in LPS-treated Jα18$^{-/-}$ mice were markedly downregulated when compared with LPS-injected WT mice; however, they were still significantly higher than those in LPS-treated Jα18$^{-/-}$ mice at the dose of 50 μg/kg and in the two control PBS groups (Table II).

Comparison of CD40, CD80, and CD86 expression on decidual DCs

To further explore the possible impact of iNKT cells on decidual DCs, we evaluated the expression of costimulatory molecules CD40, CD80, and CD86 on decidual DCs from Jα18$^{-/-}$ mice and WT mice. There were no significant differences in the CD40, CD80, and CD86 expression levels on decidual DCs between PBS-treated Jα18$^{+/+}$ mice and PBS-treated Jα18$^{-/-}$ mice. The percentages of decidual CD40$^+$, CD80$^+$ and CD86$^+$ cells in the CD11c$^+$ cell population from LPS-injected Jα18$^{+/+}$ mice were significantly higher than those from PBS-injected Jα18$^{+/+}$ and Jα18$^{-/-}$ mice. The percentages of decidual CD40$^+$, CD80$^+$, and CD86$^+$ cells in the CD11c$^+$ population from LPS-treated Jα18$^{-/-}$ mice were significantly lower than those in LPS-treated Jα18$^{+/+}$ mice (Table III).

Analysis of cytokines in the culture supernatants of decidual mononuclear cells

To better understand the mechanism by which iNKT cells affect LPS-induced preterm delivery and fetal death, the levels of Th1 and Th2 cytokines in the culture supernatants of decidual mononuclear cells from Jα18$^{-/-}$ mice and WT mice were investigated. No significant differences were observed in the concentrations of IFN-γ, IL-12p70, IL-4, and IL-10 between PBS-treated Jα18$^{+/+}$ mice and PBS-treated Jα18$^{-/-}$ mice. However, the concentrations of Th1 cytokines IFN-γ and IL-12p70 in the culture supernatants of decidual mononuclear cells from LPS-injected WT mice were apparently upregulated when compared with the two control PBS groups. The concentrations of IFN-γ and IL-12p70 in the culture supernatants were significantly lower in LPS-treated Jα18$^{-/-}$ mice than in LPS-treated Jα18$^{+/+}$ mice. In contrast, the concentrations of Th2 cytokines IL-4 and IL-10 in the supernatants from LPS-treated Jα18$^{-/-}$ mice showed no difference from those of LPS-treated Jα18$^{+/+}$ mice (Fig. 4).

Comparison of the percentages of activated decidual DC, T cell, B cell, and NK cell populations between preterm delivered mice and normally delivered mice

To further investigate the mechanisms of preterm delivery, we pooled the decidua of LPS-induced preterm delivered Jα18$^{+/+}$ mice and Jα18$^{-/-}$ mice and pooled the decidua of LPS-injected but normally delivered Jα18$^{+/+}$ mice and Jα18$^{-/-}$ mice ($n = 4$ for each group). We compared the percentages of activated DCs, T cells, B cells, and NK cells from LPS-induced preterm delivered WT and null mice with those from LPS-treated but normally delivered WT and null mice. PBS-treated WT and null mice were used as controls. There were no substantial differences in the percentages of decidual DCs, T cells, B cells, and NK cells among the LPS-injected but normally delivered mice, in either Jα18$^{+/+}$ mice or Jα18$^{-/-}$ mice. The percentages of activated decidual DCs, T cells, and NK cells from LPS-induced preterm labor mice were increased to a significantly higher level than those from the control PBS groups and LPS-treated but normally delivered Jα18$^{+/+}$ and Jα18$^{-/-}$ mice (Fig. 5).

Table II. Comparison of the percentages of activated decidual DC, T cell, B cell, and NK cell populations

Group	Mice	LPS	Activated DCs	Activated T Cells	Activated B Cells	Activated NK Cells
A	Jα18$^{+/+}$	PBS	9.3 ± 1.5	9.0 ± 1.4	6.4 ± 0.9	7.2 ± 1.3
B	Jα18$^{-/-}$	PBS	9.5 ± 1.3	8.8 ± 1.5	5.8 ± 0.6	6.9 ± 1.1
C	Jα18$^{+/+}$	50 μg/kg	25.4 ± 2.7^{a,b}	20.5 ± 2.4^{a,b}	6.1 ± 1.1	26.9 ± 2.8^{a,b}
D	Jα18$^{-/-}$	50 μg/kg	9.3 ± 1.7^{c}	9.1 ± 1.4^{c}	5.9 ± 0.9	7.3 ± 1.0^{c}
E	Jα18$^{+/+}$	100 μg/kg	39.4 ± 4.1^{a,b,c}	49.3 ± 5.1^{a,b,c}	6.8 ± 1.0	61.5 ± 5.7^{a,b,c}
F	Jα18$^{-/-}$	100 μg/kg	19.3 ± 2.9^{a,b,d,e}	18.5 ± 2.6^{a,b,d,e}	6.6 ± 0.8	22.2 ± 2.7^{a,b,d,e}

Pregnant Jα18$^{+/+}$ and Jα18$^{-/-}$ mice were i.p. injected with PBS or LPS (50 or 100 μg/kg body weight). In flow cytometric analysis, CD45$^+$ cells were gated, and the percentages of CD11c$^+$CD69$^+$ cells in the CD11c$^+$ cell population, CD3$^+$CD69$^+$ cells in the CD3$^+$ cell population, CD19$^+$CD69$^+$ cells in the CD19$^+$ cell population, and CD49b$^+$CD69$^+$ cells in the CD49b$^+$ cell population were calculated. Values represent means ± SD ($n = 4$ for each group).

[a] $p < 0.01$ versus group A.
[b] $p < 0.01$ versus group B.
[c] $p < 0.01$ versus group C.
[d] $p < 0.01$ versus group D.
[e] $p < 0.01$ versus group E.

Table III. Comparison of CD40, CD80, and CD86 expression on decidual DCs (%)

Group	Mice	Stimulator	CD40	CD80	CD86
A	Jα18$^{+/+}$	PBS	19.9 ± 3.2	23.5 ± 2.5	18.2 ± 2.3
B	Jα18$^{-/-}$	PBS	19.7 ± 2.7	24.2 ± 3.2	18.5 ± 2.9
C	Jα18$^{+/+}$	LPS	47.4 ± 5.8^{a,b}	50.9 ± 4.2^{a,b}	61.7 ± 5.7^{a,b}
D	Jα18$^{-/-}$	LPS	21.9 ± 3.0^{c}	25.6 ± 2.9^{c}	18.7 ± 2.3^{c}

Pregnant Jα18$^{-/-}$ and Jα18$^{+/+}$ mice were i.p. injected with PBS or LPS at 50 μg/kg body weight. Decidual mononuclear cells were isolated and incubated with fluorescence-conjugated anti-CD45, anti-CD11c, anti-CD40, anti-CD80, and anti-CD86 mAbs and isotype controls. The CD45$^+$ cells were gated, and the percentages of decidual CD40$^+$ cells, CD80$^+$ cells, and CD86$^+$ cells in the CD11c$^+$ cell population were calculated. Data represent means ± SD of four samples in each group.
$^a p < 0.01$ versus group A.
$^b p < 0.01$ versus group B.
$^c p < 0.01$ versus group C.

Discussion

The presence of iNKT cells at human decidua and their specific ligand CD1d at placenta villous and extravillous trophoblasts indicates that these cells may have an immunoregulatory role at the maternal/fetal interface (24, 25). Murine Vα14 NKT cells were found to accumulate in the decidua during pregnancy and induce abortion upon stimulation with their specific ligand, α-galactosylceramide, by perforin-dependent killing and production of IFN-γ and TNF-α (21, 26). Additionally, *Salmonella* LPS can stimulate iNKT cells dependent on TLR engagement of the APCs and recognition of a self glycolipid by the iNKT TCR (17). Furthermore, *Escherichia* LPS can drive iNKT cell production of IFN-γ via IL-12 and IL-18 production by activation of APCs independently of CD1d (27). These reports suggest that decidual iNKT cells may be activated indirectly by pathogen-related molecules such as bacterial LPS at the maternal/fetal interface, subsequently activating immune cell types, producing massive amounts of cytokines and playing a regulatory role in infection-associated abortion or preterm birth.

We previously reported that LPS treatment significantly increases the incidence of preterm delivery and fetal death and enhances expression of placental costimulatory molecule CD86 and activation molecule CD69 (18). In this study, we investigated the effect of iNKT cell deficiency on LPS-induced preterm birth and fetal demise. First, we showed that there was no difference in the gestation length of Jα18$^{+/+}$ mice and Jα18$^{-/-}$ mice. LPS given i.p. at 50 μg/kg body weight caused a ˃50% preterm birth rate in Jα18$^{+/+}$ mice. Therefore, it was concluded that the deficiency of iNKT cells decreased LPS-induced preterm birth and fetal demise. Alternatively, iNKT cells appear unnecessary for normal term delivery, since the gestation length was unchanged in Jα18 null mutant mice administered PBS.

LPS was also infused at 100 μg/kg body weight to determine whether iNKT cell depletion remained protective in the event of a stronger inflammatory challenge and was found to cause preterm delivery in 100% of Jα18$^{+/+}$ mice. Thus, deficiency of iNKT cells still reduced LPS-induced preterm birth and fetal demise with a high dose of LPS. Collectively, our results suggest that iNKT cells may have an important and essential role in inflammation-induced preterm birth. To our knowledge, this is the first study to address the role of iNKT cells in infection-associated preterm birth.

In the present study, we found that CD3$^+$CD49b$^+$ iNKT cells were absent or nearly undectable in Jα18$^{-/-}$ mice. In our investigation of the signaling mechanism by which iNKT cells mediate infection-associated preterm birth, we demonstrated that the expression of costimulatory molecules CD40, CD80, CD86, and CD69 in decidual DCs from iNKT cell-deficient Jα18$^{-/-}$ mice decreased significantly in comparison with those from Jα18$^{+/+}$ mice.

During pregnancy, the precise regulation of innate and adaptive immunity at the maternal/fetal interface is required to maintain the survival of the semiallogeneic embryo. At the same time, effective immunity must be maintained at the mucosal border to protect both mother and fetus from harmful pathogens. DCs are a heterogeneous population of cells that initiate and coordinate the innate and

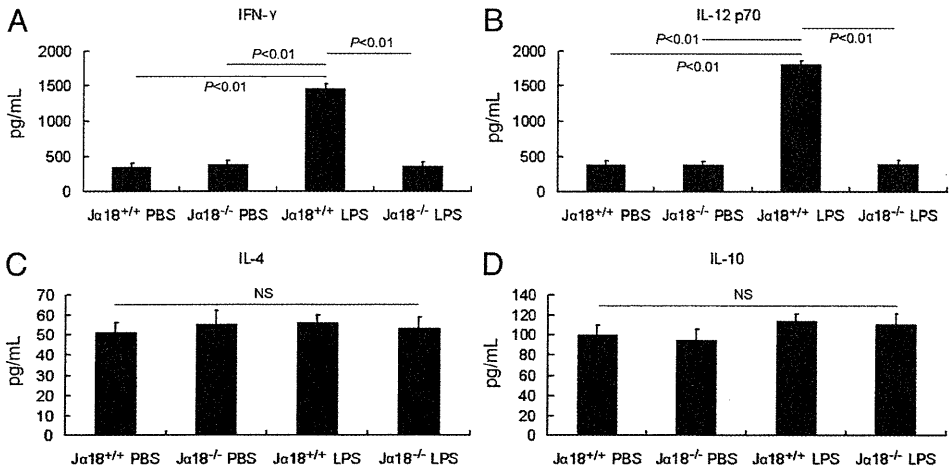

FIGURE 4. Analysis of cytokines in the culture supernatants of decidual mononuclear cells. Pregnant Jα18$^{-/-}$ or WT mice were injected i.p. with LPS to establish the preterm delivery model. Decidual mononuclear cells were isolated and cultured for 24 h. The culture supernatants were collected and stored at −80°C for cytokine assays. The concentrations of IFN-γ (**A**), IL-12p70 (**B**), IL-4 (**C**), and IL-10 (**D**) were determined by ELISA. Results are shown as means ± SD (n = 4 for each group).

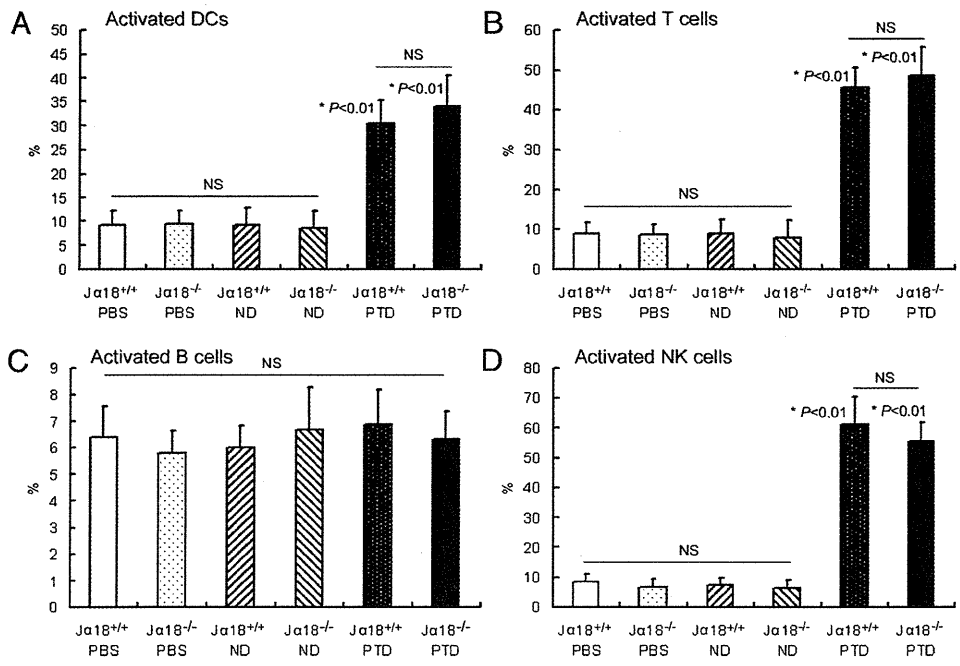

FIGURE 5. Comparison of the percentages of activated decidual DCs (**A**), T cells (**B**), B cells (**C**), and NK cells (**D**) between preterm delivery (PTD) and normal delivery (ND) mice. PBS-treated Jα18$^{+/+}$ and Jα18$^{-/-}$ mice were used as controls. Decidual tissues of LPS-treated PTD and ND mice were separated and examined respectively by flow cytometry ($n = 4$ for each group). *$p < 0.01$ compared with PBS-treated Jα18$^{+/+}$ and Jα18$^{-/-}$ mice as well as LPS-treated but ND Jα18$^{+/+}$ and Jα18$^{-/-}$ mice.

adaptive immune responses. Maternal DCs are scattered throughout the decidualized endometrium during all stages of pregnancy and appear to be important players in this fetal/maternal immune adjustment (28). Depletion of DCs has been shown to prevent blastocyst implantation and decidua formation, suggesting that uterine DCs are necessary for decidualization and affect the angiogenic response by inhibiting blood vessel maturation (29). Additionally, recent evidence points to a pivotal role of DCs in shaping the cytokine profile toward the establishment of a tolerogenic microenvironment at the maternal/fetal interface (30). Although DCs contribute to an immunosuppressive atmosphere over the course of gestation, they possess the capacity to contribute to proinflammatory responses upon pathogenic activation. Driven by pathogens and inflammatory signals, DCs undergo a complex maturation process, which not only leads to enhanced expression of costimulatory molecules and increased formation of stable MHC/peptide complexes but also to cytokine secretion modulating T cell activation and expansion, synthesis of chemokines and chemokine receptors, and regulation of T cell and DC trafficking (31). In our study, depletion of iNKT cells decreased the expression of costimulatory molecules CD40, CD80, and CD86 in decidual DCs and the number of activated decidual DCs, suggesting that iNKT cells have an impact on inflammation-induced decidual DC maturation and activation.

Productive activation of T cells occurs after concomitant engagement of TCR with Ag presented on DCs in association with MHC molecules and the delivery of costimulatory signals resulting from the interaction of CD80, CD86 with CD28, and CD40 with CD40L on the cell surface of T cells (32). Ag-specific T cell activation is a critical step in the rejection of transplanted allografts. As expected, our experiments demonstrated that decreased expression of decidual costimulatory molecules CD40, CD80, and CD86, as well as reduced activation of DCs, was consistent with downregulated decidual T cells and activated T cells. That the absence of iNKT cells decreased the numbers of T cells and activated T cells in decidua indicated that iNKT cells play a role in LPS-stimulated T cell expansion and activation.

Additionally, there were decreased numbers of NK cells and activated NK cells at the maternal/fetal interface of iNKT cell-deficient Jα18$^{-/-}$ mice in comparison with Jα18$^{+/+}$ mice, demonstrating that iNKT cells have an effect on infection-associated decidual NK cell expansion and activation. NK cells are lymphocytes characterized by high cytolytic potential against virus-infected and tumor-transformed cells. They play a fundamental role in the innate immune response through their ability to secrete cytokines and kill target cells without prior sensitization. Decidual NK cell cytolytic function is much reduced despite the presence of several activating receptors and the essential machinery required for lysis (33). Although decidual NK cell potential functions at the maternal/fetal interface are not yet clearly established, several hypotheses are being evaluated. It was proposed that NK cells in human decidua have a role in regulating trophoblast invasion by the production of IL-8 and IFN-inducible protein-10 chemokines (34). Furthermore, decidual NK cells secrete a potent array of angiogenic factors that induce vascular growth essential for the establishment of an adequate decidua (35, 36). Alternatively, we and others have proposed that those cells can become cytotoxic in nature in the presence of certain pathogens and ultimately lead to preterm birth (18, 37, 38). In our study, lack of iNKT cells caused downregulation of the NK cell population and activated NK cell proportion at the maternal/fetal interface, indicating that iNKT cells influence inflammation-induced decidual NK cell activation and cytotoxicity.

The conceptus is considered a semiallograft due to the presence of paternal HLA-C molecules. These alloantigens can be processed by maternal APCs, which present them to specific maternal CD4$^+$ T cells. After activation, the maternal CD4$^+$ T cells can become effector CD4$^+$ T cells, which are able to release various cytokines. CD4$^+$ helper T cells play important roles in an immune response to the Ag by modulating Ab production by B cells and the func-

tion of cytotoxic T cells (39). T cell immunity is classified into Th1 and Th2 types by the cytokine profile. Th1-type cytokines that promote allograft rejection may compromise pregnancy, whereas the Th2 type cytokines that inhibit Th1 responses promote allograft tolerance and therefore may improve fetal survival (40). In our experiments, the levels of Th1 cytokines IFN-γ and IL-12p70 in the culture supernatants of decidual mononuclear cells from $J\alpha18^{-/-}$ mice were obviously decreased compared with those of $J\alpha18^{+/+}$ mice, whereas the concentrations of Th2 cytokines IL-4 and IL-10 were not markedly different. These results suggest that the absence of iNKT cells relieves the shift of infection-associated Th1/Th2 balance to a Th1 predominant state, thus promoting allograft tolerance.

The cause of preterm delivery is multifactorial (24), but chorioamnionitis and infection are major causes of preterm delivery <30 wk gestation in humans. In the present study, we did not find any significant difference in the percentages of peripheral blood DCs, T cells, B cells, and NK cells among PBS-injected or LPS-injected $J\alpha18^{+/+}$ mice and $J\alpha18^{-/-}$ mice. Our findings suggest that iNKT cells have a minor effect on systemic immune cells. To further explore the cause of preterm delivery, we compared the expression of CD69 on decidual DC, T cell, B cells, and NK cell populations among LPS-induced preterm delivered and LPS-treated but normally delivered $J\alpha18^{+/+}$ and $J\alpha18^{-/-}$ mice. Preterm delivered mice showed increased activation of DCs, T cells, and NK cells at the maternal/fetal interface in comparison with normally delivered mice, suggesting an essential role of those activated immune cells for infection-induced preterm delivery. Furthermore, the deficiency of iNKT cells decreased activation of decidual DCs, T cells, and NK cells, suggesting that iNKT cells may play a key role for activation of those immune cells in chorioamnionitis-induced preterm delivery. Our findings in mice altogether suggest that iNKT cells may play an important role in inflammation-induced preterm delivery, and in future studies we will investigate whether iNKT cells may also play such a role in humans.

Disclosures

The authors have no financial conflicts of interest.

References

1. Beck, S., D. Wojdyla, L. Say, A. P. Betran, M. Merialdi, J. H. Requejo, C. Rubens, R. Menon, and P. F. Van Look. 2010. The worldwide incidence of preterm birth: a systematic review of maternal mortality and morbidity. *Bull. World Health Organ.* 88: 31–38.
2. Goldenberg, R. L., J. F. Culhane, J. D. Iams, and R. Romero. 2008. Epidemiology and causes of preterm birth. *Lancet* 371: 75–84.
3. Moster, D., R. T. Lie, and T. Markestad. 2008. Long-term medical and social consequences of preterm birth. *N. Engl. J. Med.* 359: 262–273.
4. Aarnoudse-Moens, C. S., D. P. Smidts, J. Oosterlaan, H. J. Duivenvoorden, and N. Weisglas-Kuperus. 2009. Executive function in very preterm children at early school age. *J. Abnorm. Child Psychol.* 37: 981–993.
5. Anderson, P. J., and L. W. Doyle. 2008. Cognitive and educational deficits in children born extremely preterm. *Semin. Perinatol.* 32: 51–58.
6. Li, W., E. Unlugedik, A. D. Bocking, and J. R. Challis. 2007. The role of prostaglandins in the mechanism of lipopolysaccharide-induced proMMP9 secretion from human placenta and fetal membrane cells. *Biol. Reprod.* 76: 654–659.
7. Wang, X., H. Hagberg, C. Mallard, C. Zhu, M. Hedtjärn, C. F. Tiger, K. Eriksson, A. Rosen, and B. Jacobsson. 2006. Disruption of interleukin-18, but not interleukin-1, increases vulnerability to preterm delivery and fetal mortality after intrauterine inflammation. *Am. J. Pathol.* 169: 967–976.
8. Adams Waldorf, K. M., D. Persing, M. J. Novy, D. W. Sadowsky, and M. G. Gravett. 2008. Pretreatment with Toll-like receptor 4 antagonist inhibits lipopolysaccharide-induced preterm uterine contractility, cytokines, and prostaglandins in rhesus monkeys. *Reprod. Sci.* 15: 121–127.
9. Koga, K., I. Cardenas, P. Aldo, V. M. Abrahams, B. Peng, S. Fill, R. Romero, and G. Mor. 2009. Activation of TLR3 in the trophoblast is associated with preterm delivery. *Am. J. Reprod. Immunol.* 61: 196–212.
10. Ilievski, V., and E. Hirsch. 2010. Synergy between viral and bacterial toll-like receptors leads to amplification of inflammatory responses and preterm labor in the mouse. *Biol. Reprod.* 83: 767–773.
11. Matsuda, J. L., T. Mallevaey, J. Scott-Browne, and L. Gapin. 2008. CD1d-restricted iNKT cells, the "Swiss-Army knife" of the immune system. *Curr. Opin. Immunol.* 20: 358–368.
12. Borg, N. A., K. S. Wun, L. Kjer-Nielsen, M. C. Wilce, D. G. Pellicci, R. Koh, G. S. Besra, M. Bharadwaj, D. I. Godfrey, J. McCluskey, and J. Rossjohn. 2007. CD1d-lipid-antigen recognition by the semi-invariant NKT T-cell receptor. *Nature* 448: 44–49.
13. Teige, A., R. Bockermann, M. Hasan, K. E. Olofsson, Y. Liu, and S. Issazadeh-Navikas. 2010. CD1d-dependent NKT cells play a protective role in acute and chronic arthritis models by ameliorating antigen-specific Th1 responses. *J. Immunol.* 185: 345–356.
14. Emoto, M., T. Yoshida, T. Fukuda, I. Kawamura, M. Mitsuyama, E. Kita, R. Hurwitz, S. H. Kaufmann, and Y. Emoto. 2010. α-Galactosylceramide promotes killing of *Listeria monocytogenes* within the macrophage phagosome through invariant NKT-cell activation. *Infect. Immun.* 78: 2667–2676.
15. Nowak, M., M. S. Arredouani, A. Tun-Kyi, I. Schmidt-Wolf, M. G. Sanda, S. P. Balk, and M. A. Exley. 2010. Defective NKT cell activation by $CD1d^+$ TRAMP prostate tumor cells is corrected by interleukin-12 with α-galactosylceramide. *PLoS ONE* 5: e11311.
16. Mattarollo, S. R., M. Yong, L. Tan, I. H. Frazer, and G. R. Leggatt. 2010. Secretion of IFN-γ but not IL-17 by CD1d-restricted NKT cells enhances rejection of skin grafts expressing epithelial cell-derived antigen. *J. Immunol.* 184: 5663–5669.
17. Salio, M., A. O. Speak, D. Shepherd, P. Polzella, P. A. Illarionov, N. Veerapen, G. S. Besra, F. M. Platt, and V. Cerundolo. 2007. Modulation of human natural killer T cell ligands on TLR-mediated antigen-presenting cell activation. *Proc. Natl. Acad. Sci. USA* 104: 20490–20495.
18. Li, L., J. Kang, and W. Lei. 2010. Role of Toll-like receptor 4 in inflammation-induced preterm delivery. *Mol. Hum. Reprod.* 16: 267–272.
19. Taniguchi, M., H. Koseki, T. Tokuhisa, K. Masuda, H. Sato, E. Kondo, T. Kawano, J. Cui, A. Perkes, S. Koyasu, and Y. Makino. 1996. Essential requirement of an invariant Vα14 T cell antigen receptor expression in the development of natural killer T cells. *Proc. Natl. Acad. Sci. USA* 93: 11025–11028.
20. Cui, J., T. Shin, T. Kawano, H. Sato, E. Kondo, I. Toura, Y. Kaneko, H. Koseki, M. Kanno, and M. Taniguchi. 1997. Requirement for Vα14 NKT cells in IL-12-mediated rejection of tumors. *Science* 278: 1623–1626.
21. Ito, K., M. Karasawa, T. Kawano, T. Akasaka, H. Koseki, Y. Akutsu, E. Kondo, S. Sekiya, K. Sekikawa, M. Harada, et al. 2000. Involvement of decidual Vα14 NKT cells in abortion. *Proc. Natl. Acad. Sci. USA* 97: 740–744.
22. Rogers, L., S. Burchat, J. Gage, M. Hasu, M. Thabet, L. Willcox, T. A. Ramsamy, and S. C. Whitman. 2008. Deficiency of invariant Vα14 natural killer T cells decreases atherosclerosis in LDL receptor null mice. *Cardiovasc. Res.* 78: 167–174.
23. Lin, Y., Y. Chen, Y. Zeng, T. Wang, and S. Zeng. 2005. Lymphocyte phenotyping and NK cell activity analysis in pregnant NOD/SCID mice. *J. Reprod. Immunol.* 68: 39–51.
24. Boyson, J. E., B. Rybalov, L. A. Koopman, M. Exley, S. P. Balk, F. K. Racke, F. Schatz, R. Masch, S. B. Wilson, and J. L. Strominger. 2002. CD1d and invariant NKT cells at the human maternal-fetal interface. *Proc. Natl. Acad. Sci. USA* 99: 13741–13746.
25. Matsumoto, J., K. Kawana, T. Nagamatsu, D. J. Schust, T. Fujii, H. Sato, H. Hyodo, T. Yasugi, S. Kozuma, and Y. Taketani. 2008. Expression of surface CD1d in the extravillous trophoblast cells of early gestational placenta is downregulated in a manner dependent on trophoblast differentiation. *Biochem. Biophys. Res. Commun.* 371: 236–241.
26. Tsuda, H., M. Sakai, T. Michimata, K. Tanebe, S. Hayakawa, and S. Saito. 2001. Characterization of NKT cells in human peripheral blood and decidual lymphocytes. *Am. J. Reprod. Immunol.* 45: 295–302.
27. Nagarajan, N. A., and M. Kronenberg. 2007. Invariant NKT cells amplify the innate immune response to lipopolysaccharide. *J. Immunol.* 178: 2706–2713.
28. Zarnani, A. H., S. M. Moazzeni, F. Shokri, M. Salehnia, and M. Jeddi-Tehrani. 2007. Kinetics of murine decidual dendritic cells. *Reproduction* 133: 275–283.
29. Plaks, V., T. Birnberg, T. Berkutzki, S. Sela, A. BenYashar, V. Kalchenko, G. Mor, E. Keshet, N. Dekel, M. Neeman, and S. Jung. 2008. Uterine DCs are crucial for decidua formation during embryo implantation in mice. *J. Clin. Invest.* 118: 3954–3965.
30. Laskarin, G., U. Kämmerer, D. Rukavina, A. W. Thomson, N. Fernandez, and S. M. Blois. 2007. Antigen-presenting cells and materno-fetal tolerance: an emerging role for dendritic cells. *Am. J. Reprod. Immunol.* 58: 255–267.
31. Kopcow, H. D., and S. A. Karumanchi. 2007. Angiogenic factors and natural killer (NK) cells in the pathogenesis of preeclampsia. *J. Reprod. Immunol.* 76: 23–29.
32. Hancock, W. W., M. H. Sayegh, X. G. Zheng, R. Peach, P. S. Linsley, and L. A. Turka. 1996. Costimulatory function and expression of CD40 ligand, CD80, and CD86 in vascularized murine cardiac allograft rejection. *Proc. Natl. Acad. Sci. USA* 93: 13967–13972.
33. Vacca, P., C. Cantoni, M. Vitale, C. Prato, F. Canegallo, D. Fenoglio, N. Ragni, L. Moretta, and M. C. Mingari. 2010. Crosstalk between decidual NK and $CD14^+$ myelomonocytic cells results in induction of Tregs and immunosuppression. *Proc. Natl. Acad. Sci. USA* 107: 11918–11923.
34. Hanna, J., D. Goldman-Wohl, Y. Hamani, I. Avraham, C. Greenfield, S. Natanson-Yaron, D. Prus, L. Cohen-Daniel, T. I. Arnon, I. Manaster, et al. 2006. Decidual NK cells regulate key developmental processes at the human fetal-maternal interface. *Nat. Med.* 12: 1065–1074.
35. Kalkunte, S. S., T. F. Mselle, W. E. Norris, C. R. Wira, C. L. Sentman, and S. Sharma. 2009. Vascular endothelial growth factor C facilitates immune tol-